



Circumstellar Medium Constraints on the Environment of Two Nearby Type Ia Supernovae: SN 2017cbv and SN 2020nlb

D. J. Sand¹, S. K. Sarbadhikary², C. Pellegrino^{3,4}, K. Misra⁵, R. Dastidar⁵, P. J. Brown^{6,7}, K. Itagaki⁸, S. Valenti⁹, Jonathan J. Swift¹⁰, J. E. Andrews¹¹, K. A. Bostroem⁹, J. Burke^{3,4}, L. Chomiuk², Y. Dong⁹, L. Galbany¹², M. L. Graham¹³, D. Hiramatsu^{3,4}, D. A. Howell³, E. Y. Hsiao¹⁴, D. Janzen¹⁵, J. E. Jencson¹, M. J. Lundquist¹, C. McCully^{3,4}, D. Reichart¹⁶, Nathan Smith¹, Lingzhi Wang^{17,18}, and S. Wyatt¹

¹ Steward Observatory, University of Arizona, 933 North Cherry Avenue, Tucson, AZ 85721-0065, USA; dsand@arizona.edu

² Department of Physics and Astronomy, Michigan State University, East Lansing, MI:48824, USA

³ Las Cumbres Observatory, 6740 Cortona Drive, Suite 102, Goleta, CA 93117-5575, USA

⁴ Department of Physics, University of California, Santa Barbara, CA 93106-9530, USA

⁵ Aryabhata Research Institute of Observational Sciences, Manora Peak, Nainital 263 001, India

⁶ Department of Physics and Astronomy, Texas A&M University, 4242 TAMU, College Station, TX 77843, USA

⁷ George P. and Cynthia Woods Mitchell Institute for Fundamental Physics & Astronomy

⁸ Itagaki Astronomical Observatory, Yamagata 990-2492, Japan

⁹ Department of Physics and Astronomy, University of California, 1 Shields Avenue, Davis, CA 95616-5270, USA

¹⁰ Thacher Observatory, Thacher School, 5025 Thacher Road, Ojai, CA 93023, USA

¹¹ Gemini Observatory/NSFs NOIRLab, 670 N. Aohoku Place, Hilo, HI, 96720, USA

¹² Institute of Space Sciences (ICE, CSIC), Campus UAB, Carrer de Can Magrans, s/n, E-08193 Barcelona, Spain

¹³ DiRAC Institute, Department of Astronomy, University of Washington, Box 351580, U.W., Seattle, WA 98195, USA

¹⁴ Department of Physics, Florida State University, 77 Chieftan Way, Tallahassee, FL 32306, USA

¹⁵ Department of Physics and Engineering Physics, University of Saskatchewan, 116 Science Place, Saskatoon, SK S7N 5E2, Canada

¹⁶ Department of Physics and Astronomy, University of North Carolina at Chapel Hill, Chapel Hill, NC 27599, USA

¹⁷ Chinese Academy of Sciences South America Center for Astronomy, National Astronomical Observatories, CAS, Beijing 100101, People's Republic of China

¹⁸ CAS Key Laboratory of Optical Astronomy, National Astronomical Observatories, Chinese Academy of Sciences, Beijing 100101, People's Republic of China

Received 2021 August 4; revised 2021 August 22; accepted 2021 August 23; published 2021 November 16

Abstract

We present deep Chandra X-ray observations of two nearby Type Ia supernovae, SN 2017cbv and SN 2020nlb, which reveal no X-ray emission down to a luminosity $L_X \lesssim 5.3 \times 10^{37}$ and $\lesssim 5.4 \times 10^{37}$ erg s^{−1} (0.3–10 keV), respectively, at ∼16–18 days after the explosion. With these limits, we constrain the pre-explosion mass-loss rate of the progenitor system to be $\dot{M} < 7.2 \times 10^{-9}$ and $< 9.7 \times 10^{-9} M_\odot \text{ yr}^{-1}$ for each (at a wind velocity $v_w = 100 \text{ km s}^{-1}$ and a radius of $R \approx 10^{16} \text{ cm}$), assuming any X-ray emission would originate from inverse Compton emission from optical photons upscattered by the supernova shock. If the supernova environment was a constant-density medium, we would find a number density limit of $n_{\text{CSM}} < 36$ and $< 65 \text{ cm}^{-3}$, respectively. These X-ray limits rule out all plausible symbiotic progenitor systems, as well as large swathes of parameter space associated with the single degenerate scenario, such as mass loss at the outer Lagrange point and accretion winds. We also present late-time optical spectroscopy of SN 2020nlb, and set strong limits on any swept up hydrogen ($L_{\text{H}\alpha} < 2.7 \times 10^{37} \text{ erg s}^{-1}$) and helium ($L_{\text{He}, \lambda 6678} < 2.7 \times 10^{37} \text{ erg s}^{-1}$) from a nondegenerate companion, corresponding to $M_H \lesssim 0.7\text{--}2 \times 10^{-3} M_\odot$ and $M_{\text{He}} \lesssim 4 \times 10^{-3} M_\odot$. Radio observations of SN 2020nlb at 14.6 days after explosion also yield a non-detection, ruling out most plausible symbiotic progenitor systems. While we have doubled the sample of normal Type Ia supernovae with deep X-ray limits, more observations are needed to sample the full range of luminosities and subtypes of these explosions, and set statistical constraints on their circumbinary environments.

Unified Astronomy Thesaurus concepts: Type Ia supernovae (1728); Circumstellar matter (241)

Supporting material: data behind figures

1. Introduction

Despite their critical use for cosmology, the exact progenitor systems and explosion mechanisms for Type Ia supernovae (SNe Ia) are still being determined (e.g., Jha et al. 2019, for a recent review). There are two general categories of SNe Ia progenitors that could plausibly explain how the carbon-oxygen white dwarf accretes the necessary mass to cause an explosion: the single degenerate (SD) and double degenerate (DD) scenarios. In the DD scenario, a second degenerate companion (i.e., another white dwarf), is in the binary system (Iben & Tutukov 1984; Webbink 1984), while in the SD scenario there is a nondegenerate companion star (Whelan & Iben 1973). Within these two broad categories, the exact

triggering mechanism for the thermonuclear explosion is a topic of current research.

There are several observational techniques that have been developed to shed light on the progenitor system, although we only mention a few here. For instance, models predict that the very early light curves of SNe Ia may exhibit a *blue bump* in the UV optical in the days after explosion due to the ejecta shocking the nondegenerate companion (Kasen 2010). A similar signature has been observed in a handful of instances (e.g., Cao et al. 2015; Marion et al. 2016; Hosseinzadeh et al. 2017a; Miller et al. 2018; Dimitriadis et al. 2019; Shappee et al. 2019; Miller et al. 2020; Tucker et al. 2021; Burke et al. 2021, and strongly constrained in other instances, e.g., Hayden et al. 2010; Bianco et al. 2011; Ganeshalingam et al. 2011; Brown

et al. 2012; Olling et al. 2015), although the interpretation of these early light curves are still a matter of debate. Meanwhile, another prediction of the SD scenario is that material stripped from the companion star is swept up by the SN Ia ejecta, detectable as a narrow emission line of hydrogen or helium at late times (most recently, Botyánszki et al. 2018; Dessart et al. 2020). While most searches have only led to limits on the amount of stripped hydrogen and/or helium (Mattila et al. 2005; Leonard 2007; Shappee et al. 2013; Lundqvist et al. 2013, 2015; Maguire et al. 2016; Graham et al. 2017; Shappee et al. 2018; Holmbo et al. 2019; Tucker et al. 2019; Dimitriadis et al. 2019; Sand et al. 2016, 2018, 2019; Tucker et al. 2020), three recent detections from fast-declining SNe Ia (Kollmeier et al. 2019; Valley et al. 2019; Prieto et al. 2020; Elias-Rosa et al. 2021) indicate that a broader search for such features may prove fruitful. Presumably, if an early light-curve bump was due to interaction with a nondegenerate companion, then at late times a hydrogen or helium emission line should be visible. Such important cross checks between early light-curve and nebular signatures of the progenitor are essential, as has recently been carried out for SN 2017cbv (early light curve: Hosseinzadeh et al. 2017a; nebular spectra: Sand et al. 2018) and SN 2018oh (early light curve: Dimitriadis et al. 2019; Li et al. 2019; Shappee et al. 2019; nebular spectra: Dimitriadis et al. 2019; Tucker et al. 2019). In these recent examples, even though the early light curves may point to an SD progenitor, the nebular spectra do not necessarily corroborate this picture, suggesting that further progenitor probes are necessary to understand these systems.

One powerful probe of the immediate SN Ia environment, and thus the progenitor system, utilizes X-ray observations around the time of maximum light (Margutti et al. 2012; Horesh et al. 2012a; Margutti et al. 2014; Russell & Immler 2012; Shappee et al. 2018, 2019; Stauffer et al. 2021). X-ray emission in the weeks after an SN Ia explosion originates from the upscattering of optical photons off relativistic particles accelerated at the SN shock (i.e., inverse Compton emission; Chevalier & Fransson 2006; Margutti et al. 2012). This circumstellar medium was in turn shaped by the mass loss of the progenitor star system leading up to the explosion. Broadly speaking, in the SD scenario the white dwarf accretes material from a nondegenerate stellar companion, either through direct Roche lobe overflow (RLOF; Nomoto 1982) or from a wind from the secondary star (the *symbiotic channel*; e.g., Patat et al. 2011)—it thus is expected to have residual circumstellar material (CSM) in its immediate environment either from the donor star wind or from nonconservative mass loss from the RLOF transfer. By contrast, a standard DD scenario involving two white dwarfs inspiraling due to angular momentum loss should have a *cleaner* CSM environment.

Deep Chandra X-ray limits have been reported for only two normal SNe Ia thus far—the nearby and well-studied SN 2011fe (Margutti et al. 2012) and SN 2014J (Margutti et al. 2014). Both resulted in strong X-ray upper limits, which ruled out a symbiotic giant star companion and large portions of parameter space associated with accretion winds and Lagrangian losses from a main-sequence or subgiant companion. Despite these strong results, deep X-ray data for two SNe Ia is insufficient to draw wider conclusions about the SN Ia population, and ultimately a statistical data set of deep X-ray

limits on SNe Ia is needed (along with other tracers) to constrain SN Ia progenitor properties.

Here, we present Chandra X-ray data of two nearby Type Ia SNe—SN 2017cbv and SN 2020nlb—to constrain the circumstellar environment associated with the progenitor system, doubling the sample with deep X-ray limits. The study of SN 2017cbv is particularly interesting given the *blue bump* observed in its early light curve, which may be due to interaction with a nondegenerate companion. Meanwhile, we couple deep X-ray data of SN 2020nlb with radio data from the Very Large Array (VLA) and nebular spectroscopy to constrain any hydrogen or helium emission—these complementary probes are essential for narrowing in on the SN Ia progenitor. We end this paper with our X-ray derived CSM constraints and a discussion of the donor star and allowed progenitor configuration for SN 2017cbv and SN 2020nlb.

2. Background

2.1. SN 2017cbv

SN 2017cbv (R.A. $14^{\text{h}}32^{\text{m}}34.38^{\text{s}}$ and decl. $-44^{\circ}08'03.1''$ J2000) was discovered in the outskirts of the nearby galaxy NGC 5643 on 2017 March 10 UT (MJD 57822.14) at a magnitude of $r \approx 16$ by the Distance Less Than 40 Mpc survey (Tartaglia et al. 2018). Within hours of discovery, the transient was classified as a very young SN Ia (Hosseinzadeh et al. 2017b), and an intense multiwavelength follow-up campaign was begun. The early light curve of SN 2017cbv displayed a clear, blue excess, lasting ~ 3 days (Hosseinzadeh et al. 2017a). Such excess emission is predicted in the SD scenario, when the SN ejecta shock a nondegenerate companion star (Kasen 2010). While the observed optical light curve of SN 2017cbv is well fit to this model, it overpredicts the observed flux in the ultraviolet bands (possibly due to line blanketing or other physics not currently accounted for in the models; see, Hosseinzadeh et al. 2017a). Nebular phase spectroscopy did not detect any narrow hydrogen or helium features (Sand et al. 2018), as might be expected in the SD scenario (e.g., Botyánszki et al. 2018; Dessart et al. 2020), although further modeling is needed. The uncertain origin for the early blue excess emission makes SN 2017cbv an excellent target for a deep X-ray search for CSM interaction, as a complementary probe of the progenitor system.

We adopt an explosion epoch of MJD 57821.0, as found by Hosseinzadeh et al. (2017a) based on the early Si II velocity evolution (using the technique described in Piro & Nakar 2014). We also adopt a distance of $\mu = 30.58$ mag ($D \approx 13.1$ Mpc), the value used by Wang et al. (2020) for presenting their SN 2017cbv bolometric light curve, which we adopt for our analysis as well. This distance is in agreement with other recent light-curve analyses of SN 2017cbv (e.g., Sand et al. 2018; Burns et al. 2020), and a tip of the red-giant branch distance to SN 2017cbv’s host galaxy, NGC 5643 (Hoyt et al. 2021). We also use the epoch of *B*-band maximum from Wang et al. (2020) for reference, MJD 57840.87.

The Galactic neutral hydrogen column density in the direction of SN 2017cbv is $N_{\text{H}} = 8.014 \times 10^{20} \text{ cm}^{-2}$ (Kalberla et al. 2005). The hydrogen column associated with the host galaxy is likely negligible, as no significant host galaxy extinction is evident (see discussions in Ferretti et al. 2017; Sand et al. 2018); we therefore adopt $N_{\text{H}} = 8.014 \times 10^{20} \text{ cm}^{-2}$

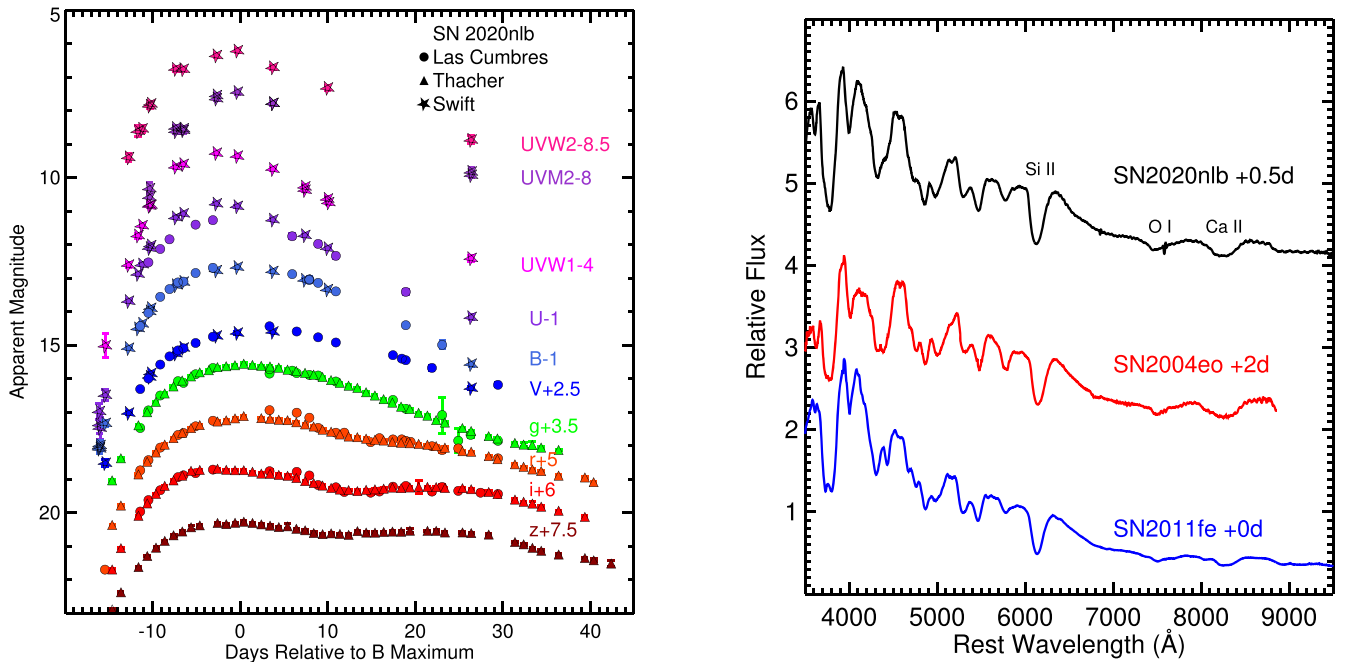


Figure 1. Left: Swift UVOT, Thacher, and Las Cumbres Observatory optical photometry of SN 2020nlb, spanning out to ~ 30 days after B -band maximum. The light curves have not been corrected for Milky Way extinction in this plot. The light curve will be made available in electronic format upon publication. Right: the +0.5 day spectrum of SN 2020nlb, along with spectra of SN 2004eo (+2 days; Pastorello et al. 2007) and the canonical *normal* Type Ia SN 2011fe (+0 day; Pereira et al. 2013). The SN 2020nlb data shown in these panels is available as the data behind the figure.

(The data used to create this figure are available.)

as the total hydrogen column density to SN 2017cbv in this work.

2.2. SN 2020nlb

SN 2020nlb was discovered on 2020 June 25.25 UT (MJD 59025.25) by the Asteroid Terrestrial impact Last Alert System (ATLAS) survey (Tonry et al. 2018) with an *orange* magnitude of 17.44. The last non-detection from ATLAS was 2 days earlier (2020 June 23.28). The field of SN 2020nlb was also monitored by the Itagaki Astronomical Observatory’s 0.35 m telescope in Okayama, Japan, which obtained a tighter non-detection epoch of 2020 June 24.57 (MJD 59024.57), with a limiting magnitude of < 18.5 mag, before also detecting the SN on 2020 June 26.56 at 16.1 mag. The unfiltered Itagaki photometry was extracted using *Astrometrica* (Raab 2012) and calibrated to the Fourth US Naval Observatory CCD Astrograph Catalog (Zacharias et al. 2013). We adopt the midpoint between the Itagaki non-detection and the first detection by the ATLAS survey as the explosion epoch (MJD 59024.91). Our X-ray analysis is not sensitive to the exact epoch adopted.

SN 2020nlb (RA $12^{\text{h}}25^{\text{m}}24.18^{\text{s}}$ and Dec $+18^{\circ}12'12.5''$ J2000) exploded in the halo of M85 ($v_{\odot} = 729 \text{ km s}^{-1}$, $z_{\odot} = 0.002432$; Smith et al. 2000), an early type galaxy in the Virgo Cluster. Many distance measurements to M85 have been made, but we will utilize the surface brightness fluctuation measurement from the Advanced Camera for Surveys Virgo Cluster Survey, which found a distance modulus of $\mu = 31.26 \pm 0.05$ mag ($D = 17.9$ Mpc; Mei et al. 2007). We adopt a Milky Way extinction of $E(B - V) = 0.026$ mag based on the dust maps of Schlafly & Finkbeiner (2011).

No results on SN 2020nlb have been published in the literature, and so we present UV/optical photometry and a maximum-light spectrum to characterize this SN Ia. We also present a nebular spectrum to constrain narrow hydrogen or helium emission from any companion or CSM interaction to complement the X-ray CSM constraints. A more comprehensive optical-infrared analysis of SN 2020nlb will be presented in a future work. The Galactic neutral hydrogen column density in the direction of SN 2020nlb is $N_{\text{H}} = 2.49 \times 10^{20} \text{ cm}^{-2}$ (Kalberla et al. 2005).

2.2.1. Light Curve

We display a *UBVgri* light curve of SN 2020nlb in the left panel of Figure 1, taken with the 0.4 and 1.0 m telescope network of Las Cumbres Observatory (Brown et al. 2013) as part of the Global Supernova Project (e.g., Szalai et al. 2019). These data were reduced in a standard way using the PyRAF-based photometric pipeline *lcogtsnpipe* (Valenti et al. 2016). An additional, high cadence data set was obtained by the 0.7 m Thacher Observatory (Swift & Vyhnaal 2018) in the g , r , i , z bands. The data was reduced in a standard way, and the point-spread function photometry tool *DoPHOT* (Schechter et al. 1993) was used in conjunction with photometric calibration from Panoramic Survey Telescope and Rapid Response System (Pan-STARRS) DR1 (Flewelling et al. 2020) to produce the final light curve. Since the SN was offset from the host galaxy, no image subtraction was performed, and we expect host galaxy contamination to be minimal.

Observations from the Neil Gehrels Swift Observatory (Swift; Gehrels et al. 2004a) Ultra-Violet Optical Telescope (UVOT; Roming et al. 2005) were also obtained and reduced using the pipeline associated with the Swift Optical Ultraviolet

Supernovae Archive (Brown et al. 2014) and the zero-points of Breeveld et al. (2010). The Swift data is also displayed in Figure 1.

We fit a fourth order polynomial to the B - and V -band light curve of SN 2020nlb around maximum light, resampling the data based on the photometric uncertainties over 1000 trials. We find a peak B -band apparent magnitude of $B_{\max} = 12.11 \pm 0.02$ mag on $\text{MJD} = 59041.8 \pm 0.2$ (UT 2020 July 11.8), which we adopt throughout this work. The V -band light curve peaked at $V_{\max} = 12.04 \pm 0.03$ mag on $\text{MJD} = 59043.9 \pm 0.3$, which is 2.1 days after the B -band peak. The B -band decline rate $\Delta m_{15}(B)$ is measured to be 1.29 ± 0.06 mag, based on the polynomial fit.

One way to constrain host galaxy extinction is to measure the color at maximum light, $B_{\max} - V_{\max}$, which was parameterized as a function of the decline rate parameter, $\Delta m_{15}(B)$, in Phillips et al. (1999). After applying a Milky Way extinction of $E(B - V)_{\text{MW}} = 0.026$ mag, we find $B_{\max} - V_{\max} = 0.04 \pm 0.04$ mag from the polynomial fits described in the previous paragraph. This is close to the expectation from the Phillips et al. (1999) relation ($B_{\max} - V_{\max} = -0.05 \pm 0.03$ mag), and so we consider host extinction to be minimal for this work. Any underestimate of the extinction would lead to a corresponding underestimate of the luminosity of the supernova, which ultimately would yield slightly weaker constraints on the CSM from our X-ray limits. Applying only Milky Way extinction to the observed B_{\max} , and using a distance of 17.9 Mpc, yields a peak absolute B -band magnitude of $M_B = -19.25$ mag, which is in line with SNe Ia with similar decline rates (Blondin et al. 2012; Folatelli et al. 2013).

2.2.2. Spectroscopy

In the right panel of Figure 1, we show a spectrum taken with the FLOYDS robotic spectrograph (Brown et al. 2013) at Faulkes Telescope North on 2020 July 12 06:32 UTC (+0.5 day with respect to B -band maximum), reduced with the pipeline described in Valenti et al. (2014). Using the Supernova IDentification software package (SNID; Blondin & Tonry 2007) we find that all reasonable matches correspond to SNe Ia near maximum light. A particularly good match to SN 2004eo at +2 day with respect to B -band maximum was found, with similar Si II and O I strengths between the two events. SN 2004eo also has a similar, relatively fast light-curve decline rate ($\Delta m_{15}(B) = 1.45$ mag; Pastorello et al. 2007) as SN 2020nlb ($\Delta m_{15}(B) = 1.29$ mag). We also compare the SN 2020nlb spectrum to the canonical *normal* SN Ia 2011fe at maximum light in Figure 1 for illustrative purposes.

We measure a Si II $\lambda 6355$ velocity of $10,400 \pm 100 \text{ km s}^{-1}$ near maximum light, as well as pseudo-equivalent width (pEW) values of 118 and 24 Å for the Si II $\lambda 6355$ and $\lambda 5972$ features, respectively, from the +0.5 day FLOYDS spectrum. In the standard Branch classification scheme (Branch et al. 2006), SN 2020nlb is a Core Normal supernova, and belongs to the Normal Velocity class of SNe Ia as described in Wang et al. (2009).

An additional low resolution optical spectrum was obtained with the Blue Channel spectrograph (Schmidt et al. 1989) at the MMT on 2021 January 28 21:06 UTC (+179 days), using the 3001 mm^{-1} grating and an exposure time of $3 \times 900 \text{ s}$. We display this spectrum in Figure 4, and use it in Section 5 to constrain any hydrogen or helium in the nebular phase. To

account for slit losses, we scale this spectrum to an r -band magnitude of 17.92, based on an interpolation of the Zwicky Transient Facility (ZTF; Bellm et al. 2019) light curve at late times (similar to Sand et al. 2018).

3. X-Ray Observations and Analysis

3.1. Swift-X-ray Telescope (XRT)

The Swift (Gehrels et al. 2004b) XRT (Burrows et al. 2005) observed both SN 2017cbv and SN 2020nlb extensively and we report flux limits here. All XRT data was analyzed using HEASoft (v6.28) and corresponding calibration files. Standard filtering and screening criteria were applied.

We gathered Swift XRT data of SN 2017cbv taken between 2017 March 10.5 and April 15.46, corresponding to ≈ 1.5 and 37.5 days from our adopted explosion epoch, with a total accumulated exposure time of 62.2 ks. SN 2017cbv sits in a region of low background, and we obtain an unabsorbed (accounting for Galactic absorption) 3σ flux limit of $F < 7.7 \times 10^{-15} \text{ erg cm}^{-2} \text{ s}^{-1}$ in the 0.3–10 keV energy range, corresponding to a 3σ luminosity limit of $L < 1.6 \times 10^{38} \text{ erg s}^{-1}$ at a distance of 13.1 Mpc.

A sequence of Swift XRT data was taken of SN 2020nlb (alongside the UVOT data described in Section 2.2), starting on 2020 June 25.76 UTC. We gathered all data taken through 2020 August 07.2 UTC (~ 43 days after our adopted explosion epoch), a total of 27.5 ks. Unresolved, diffuse X-ray emission from the host elliptical galaxy M85 is apparent in the combined XRT data, which largely resolves into point sources in the Chandra data presented below. At the position of SN 2020nlb, we find an unabsorbed 3σ flux limit of $F < 1.4 \times 10^{-14} \text{ erg cm}^{-2} \text{ s}^{-1}$ in the 0.3–10 keV energy range, corresponding to a 3σ luminosity limit of $L < 5.5 \times 10^{38} \text{ erg s}^{-1}$ at a distance of 17.9 Mpc.

The XRT limits we obtain are a factor of ~ 3 –10 less stringent than the Chandra data we present in the next section, and for this reason we do not consider this data further as we constrain the circumbinary environment of SN 2017cbv and SN 2020nlb.

3.2. Chandra

Deep X-ray follow-up of both SN 2017cbv and SN 2020nlb were obtained with the Chandra X-ray Observatory under Director’s Discretionary Time proposals. All data were reduced within a conda CIAO (v4.12) environment using relevant calibration files (CALDB v4.9.1) and standard ACIS data filtering. All X-ray count limits and confidence bounds are calculated assuming Poisson statistics, as described in Primi & Kashyap (2014). We present false color X-ray images, and zoom-ins on each SN location, in Figure 2.

Observations of SN 2017cbv began on 2017 March 27 (PI: Drout; Proposal 1850876; Obs ID 20055), and the total exposure time was 51 ks. The midtime of the observations ($\text{MJD} = 57839.789$) corresponds to $\delta t = 17.89$ days with respect to the explosion epoch, or -1.1 days with respect to B -band maximum. No X-ray source is detected with a 3σ upper limit of $1.8 \times 10^{-4} \text{ counts s}^{-1}$ in the 0.3–10 keV energy band, which corresponds to a flux limit of $F < 2.2 \times 10^{-15} \text{ erg cm}^{-2} \text{ s}^{-1}$, assuming a power-law model with spectral photon index $\Gamma = 2$. The unabsorbed flux limit is then $F < 2.6 \times 10^{-15} \text{ erg cm}^{-2} \text{ s}^{-1}$ ($N_{\text{H}} = 8.014 \times 10^{20} \text{ cm}^{-2}$;

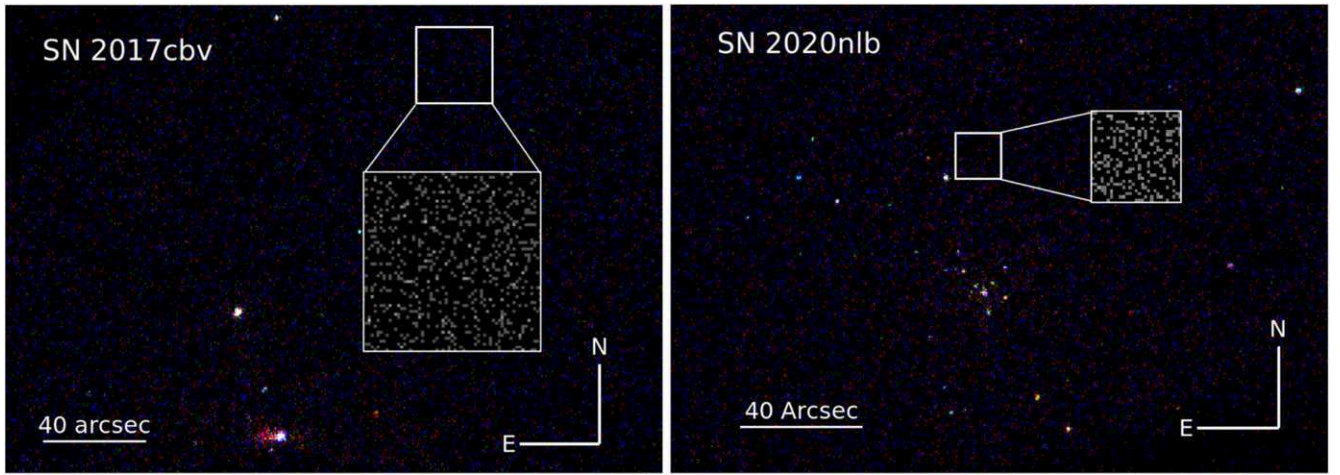


Figure 2. False color Chandra X-ray images of both SN 2017cbv (left; $\delta t = 17.89$ days after explosion) and SN 2020nlb (right; $\delta t = 15.79$ days after explosion). Red, green, and blue colors refer to soft (0.3–1.4 keV), medium (1.4–3 keV), and hard (3–10 keV) photons, respectively. The gray-scale zoom in on each panel is the full 0.3–10 keV Chandra energy range.

0.3–10 keV energy band), corresponding to a 3σ luminosity limit of $L < 5.4 \times 10^{37} \text{ erg s}^{-1}$ at a distance of 13.1 Mpc.

Chandra observations of SN 2020nlb (PI: Sand; Proposal 21508740; Obs ID 23314, 23315)¹⁹ were split into two blocks for a total exposure time of 75 ks. The first observation (totaling 63 ks) began on 2020 July 09 23:58 (UT), while the second observation (12 ks) began ~ 1.5 days after the end of the first one on 2020 July 12 04:15. We take the weighted average time of these two exposures as the effective epoch of the observations, MJD 59040.7, which corresponds to $\delta t = 15.79$ days with respect to the assumed explosion epoch, or -1.10 days with respect to B -band maximum. For our analysis, we extract the individual source spectra and use the CIAO/*specextract* task for combination of the spectra and appropriate response files. We have also combined the two observations into a single event map using the CIAO/*merge_obs* task for illustrative purposes in Figure 2, to show that no source is present. For the combined spectrum, at the position of SN 2020nlb, we find a 3σ flux limit of $F < 1.3 \times 10^{-15} \text{ erg cm}^{-2} \text{ s}^{-1}$ in the 0.3–10 keV energy range, assuming a power-law model with spectral photon index $\Gamma = 2$. The unabsorbed flux limit is then $F < 1.4 \times 10^{-15} \text{ erg cm}^{-2} \text{ s}^{-1}$ ($N_H = 2.49 \times 10^{20} \text{ cm}^{-2}$; 0.3–10 keV energy band), and the 3σ luminosity limit is $L < 5.4 \times 10^{37} \text{ erg s}^{-1}$ at a distance of 17.9 Mpc.

We place the Chandra X-ray luminosity limits of SN 2017cbv and SN 2020nlb in context in Figure 3, in comparison to the majority of X-ray limits in the literature. The data on SN 2017cbv and SN 2020nlb are among the most constraining obtained for any SNe Ia, just behind the very nearby SNe 2011fe and 2014J. We use these limits in Section 7 to constrain any CSM associated with these SNe.

4. The Bolometric Luminosity

X-ray emission in low density, hydrogen stripped progenitor systems in the first ~ 1 –2 months after explosion is dominated by inverse Compton scattering of photospheric photons by relativistic electrons accelerated by the SN shock (Chevalier & Fransson 2006; Margutti et al. 2012). The inverse Compton X-ray luminosity is proportional to the bolometric luminosity

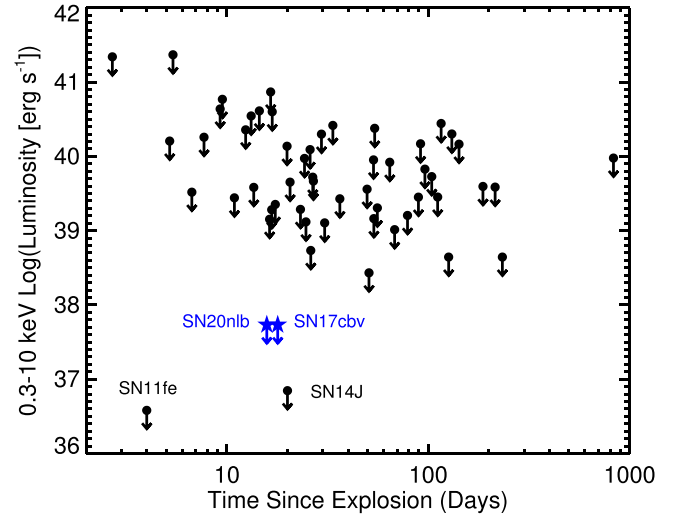


Figure 3. X-ray luminosity limits of normal SNe Ia from the compilation of Russell & Immler (2012), along with deep Chandra observations of SN 2011fe (Margutti et al. 2012) and SN 2014J (Margutti et al. 2014). The new Chandra X-ray limits for SN 2020nlb and SN 2017cbv are also shown as blue stars, and are the deepest data taken of SNe Ia beyond $D = 10$ Mpc. Note that the data from Russell & Immler (2012) is generally derived from the combination of Swift XRT data taken across many epochs over ~ 30 days, which is not well represented by the points in the plot.

of the SN, and so bolometric luminosity is a key ingredient of our analysis, which we discuss here.

We adopt the pseudo-bolometric light curve of SN 2017cbv published in (Wang et al. 2020, see their Table 7), who combined UV+optical+nearIR photometry to construct a pseudo-bolometric light curve using the SNooPy light-curve package (Burns et al. 2011, 2014); we refer the reader to that work for details. Interpolating the Wang et al. (2020) bolometric light curve to the Chandra X-ray epoch yields $L_{\text{bol}} = 1.46 \times 10^{43} \text{ erg s}^{-1}$ at our adopted distance of 13.1 Mpc.

Based on our UV+optical light curve of SN 2020nlb presented in Section 2.2.1, we construct a pseudo-bolometric light curve using the *direct* method in the SNooPy light-curve package. We use the UVW1 and UVW2 filters from Swift and the Las Cumbres UVBgr light curves for our analysis (which encompasses a broad wavelength range on one telescope

¹⁹ 10.25574/23314 and 10.25574/23315, respectively.

system), ignoring the *UVM2* filter as its light curve was lower signal to noise and sparser, making interpolation between epochs difficult. The direct method takes the flux in each filter and integrates over all filters, interpolating when necessary when a given filter is missing. The program also takes into account the extinction (where we are only considering Milky Way extinction, see Section 2.2.1) and distance to the supernova. We extrapolate the flux in the near-infrared by assuming a Rayleigh–Jeans tail, although this only has a small effect on our results. We also experimented with the *spectral energy distribution* method in SNooPy, using the Hsiao et al. (2007) spectral energy distribution templates, and obtained results consistent with the direct method to within $\sim 4\%$. Given this, we utilize the direct results and find $L_{\text{bol}} = 1.0 \times 10^{43} \text{ erg s}^{-1}$ at the epoch of the Chandra X-ray observations (MJD 59040.7).

We plot both of the bolometric light curves in the bottom panels of Figure 5, and highlight the luminosity at the epoch of the Chandra observations.

5. SN 2020nlb Progenitor Constraints from Nebular Spectroscopy

We measure complementary constraints on the progenitor system and environment of SN 2020nlb using the flux-calibrated, extinction, and redshift-corrected nebular spectrum (+179d with respect to *B*-band maximum, and +196d with respect to our adopted explosion epoch of MJD 59024.91) presented in Section 2.2.2 and shown in Figure 4, to go along with our primary X-ray results in the next section. We remind the reader that we have scaled this spectrum to $r = 17.92$ mag to match the late-time ZTF photometry to account for nonphotometric conditions and slit losses. Using similar techniques, strong constraints on H and He emission have already been placed on SN 2017cbv, using the models of Botyánszki et al. (2018), with limits of $M_{\text{H}} < 1 \times 10^{-4} M_{\odot}$ and $M_{\text{He}} < 5 \times 10^{-4} M_{\odot}$, respectively; this is ~ 3 orders of magnitude below expectations for the SD scenario (Sand et al. 2018).

If the progenitor system of SN 2020nlb had a nondegenerate companion star, then models predict that the SN ejecta will impact the companion, and manifest as narrow hydrogen (or helium) emission lines with $\text{FWHM} \approx 1000 \text{ km s}^{-1}$ at late times (e.g., Marietta et al. 2000; Mattila et al. 2005; Pan et al. 2010, 2012; Liu et al. 2012, 2013; Lundqvist et al. 2013; Botyánszki et al. 2018; Dessart et al. 2020, among others). The models for the emission from stripped material expect $\gtrsim 0.1 M_{\odot}$ of stripped hydrogen, but have considerable diversity in the strength and shape of the observed emission line, and depend on the details of the explosion and radiative transfer physics employed. Here, we will rely on the latest radiative transfer modeling and predictions from Botyánszki et al. (2018) and Dessart et al. (2020), and refer the reader to those works for details.

Careful visual inspection of Figure 4 reveals no hydrogen or helium emission features, including from the host galaxy. To set quantitative limits on narrow $\text{H}\alpha$ as well as $\text{He I } \lambda 5875 \text{ \AA}$ and $\lambda 6678 \text{ \AA}$ emission, we mimic the methodology of Sand et al. (2018, 2019), which we briefly describe here. We take the flux-calibrated, extinction, and redshift-corrected spectrum and bin to the native resolution, $\approx 6.5 \text{ \AA}$. We then establish a *continuum level* around the hydrogen and helium line wavelengths by smoothing the spectrum on scales larger than

the expected emission ($\text{FWHM} \approx 1000 \text{ km s}^{-1}$) using a second-order Savitsky–Golay filter with a width of 190 \AA . We experimented with various filter widths in order to best recover simulated emission line features in our data. Any hydrogen or helium emission line feature of the width we are interested in would be apparent in the difference between the smoothed and un-smoothed spectrum, which we refer to as the residual spectrum.

To estimate the maximum $\text{H}\alpha$ (or helium) emission that could go undetected, we directly implant emission lines into our data. We assume a line width of $\text{FWHM} \approx 1000 \text{ km s}^{-1}$ and a peak flux that is four times the rms of the residual spectrum. This results in a $\text{H}\alpha$ flux limit of $7.1 \times 10^{-16} \text{ erg s}^{-1} \text{ cm}^{-2}$, and a luminosity limit of $2.7 \times 10^{37} \text{ erg s}^{-1}$ at a distance of $D = 17.9 \text{ Mpc}$. Similarly, we find a $\text{He I } \lambda 6678 \text{ \AA}$ ($\lambda 5875 \text{ \AA}$) flux limit of $7.1 \times 10^{-16} \text{ erg s}^{-1} \text{ cm}^{-2}$ ($7.9 \times 10^{-16} \text{ erg s}^{-1} \text{ cm}^{-2}$), leading to a luminosity limit of $2.7 \times 10^{37} \text{ erg s}^{-1}$ ($3.0 \times 10^{37} \text{ erg s}^{-1}$). Dessart et al. (2020) suggest that limits on the equivalent width of the $\text{H}\alpha$ line may also be an effective way to obtain stripped-mass limits. Given this, we have also followed the Dessart et al. (2020) prescription for obtaining equivalent width limits (using their Equation (B.1)), and find $\text{EQW}(\text{H}\alpha) < 5.3 \text{ \AA}$. We illustrate our detection limits in the bottom panels of Figure 4.

The recent 3D radiation transport results of Botyánszki et al. (2018) presented simulated SN Ia spectra at 200 days after explosion (well matched to our spectrum at +196 days after explosion, which we make no further adjustments to) derived from the SN Ia ejecta-companion interaction simulations of Boehner et al. (2017), which utilized a spherically symmetric W7 explosion model (Nomoto et al. 1984; Thielemann et al. 1986). These simulated spectra show strong hydrogen and helium nebular emission ($\text{FWHM} \approx 1000 \text{ km s}^{-1}$, shifted by up to $\sim 10 \text{ \AA}$ from rest) with $L_{\text{H}\alpha} \approx 4.5\text{--}15.7 \times 10^{39} \text{ erg s}^{-1}$ for their main-sequence, subgiant, and red-giant companion star models, corresponding to $M_{\text{strip}} \sim 0.2\text{--}0.4 M_{\odot}$. Given our $\text{H}\alpha$ luminosity limit of $2.7 \times 10^{37} \text{ erg s}^{-1}$, we rule out the basic predictions of Botyánszki et al. (2018) in SN 2020nlb by over two orders of magnitude. To approximate the effects of smaller stripped hydrogen masses (due to weaker explosions, wider companion separations or inhomogeneities in the ejecta structure), Botyánszki et al. (2018) varied the hydrogen density in their fiducial main-sequence companion model, fitting a quadratic to the relation between stripped hydrogen mass and the $\text{H}\alpha$ luminosity (see their Equation (1), but note the typographical error corrected in Sand et al. 2018). Using this formula, we derive a stripped hydrogen mass limit of $M_{\text{strip}} = 7 \times 10^{-4} M_{\odot}$.

Further radiative transfer calculations of SN Ia ejecta enclosing stripped material from a nondegenerate companion star were recently performed by Dessart et al. (2020). These 1D calculations include several different delayed detonation models (DDC0, DDC15, and DDC25; Blondin et al. 2013) and a sub-Chandrasekhar model (SCH3p5; Blondin et al. 2017), expanding beyond the focus on W7 explosions in previous work. They also include non-LTE physics and optical depth effects, and cover stripped hydrogen masses from $M_{\text{strip}} \sim 0.001\text{--}0.5 M_{\odot}$ (although we note that masses in the $M_{\text{strip}} \sim 0.1\text{--}0.5 M_{\odot}$ range are what is seen in multidimensional hydrodynamic simulations, as mentioned above). We estimate hydrogen mass limits of $M_{\text{strip}} = 1\text{--}2 \times 10^{-3} M_{\odot}$ based on these models, where the range includes the three explosion

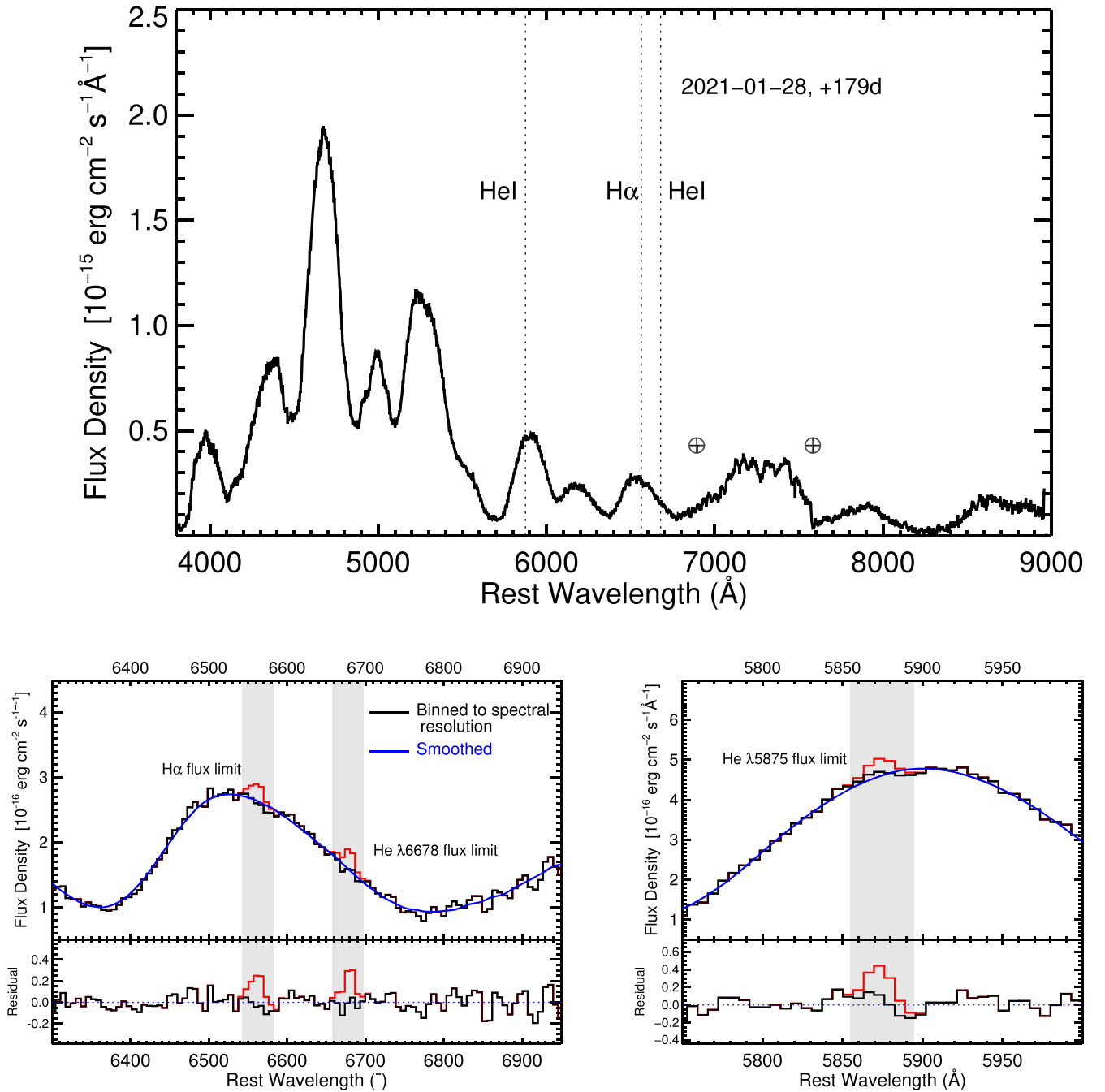


Figure 4. Top—nebular-phase spectrum of SN 2020nlb, flux calibrated and corrected for MW extinction. We mark the locations of the A- and B-band telluric features. Bottom—zoom in on the region around H α and He I $\lambda 6678$ (left) as well as He I $\lambda 5875$ (right), where we constrain any narrow emission feature by implanting simulated lines. The black histogram is the data binned to the resolution of the spectrum, while the blue shows the data smoothed by a second-order Savitsky–Golay filter. The bottom panel on each plot shows the difference between the original spectrum and the smoothed version. The red histogram is an implanted emission line feature with a peak flux four times the rms, representing the detection limit for an hydrogen or helium emission line. The gray shaded regions correspond to 1000 km s $^{-1}$ around the rest wavelength of the hydrogen and helium lines. The SN 2020nlb spectrum is available as the data behind the figure.

(The data used to create this figure are available.)

models with tabulated results in the appendix of Dessart et al. (2020). When we use our equivalent width limit for H α (EQW (H α) < 5.3 Å) instead of our luminosity limit, we obtain nearly identical hydrogen mass limits of $M_{\text{strip}} = 1\text{--}3 \times 10^{-3} M_{\odot}$. All of these mass limits are ~ 2 orders of magnitude lower than expectations from SD models.

Helium stars are also plausible white dwarf companions (e.g., Iben & Tutukov 1984), and models predict that such

progenitor systems should yield $M_{\text{strip}} \approx 0.002\text{--}0.06 M_{\odot}$ of stripped helium-rich material, which ultimately may be visible in nebular spectra (e.g., Pan et al. 2012; Liu et al. 2013). Unfortunately, few radiative transport simulations of the helium star scenario have been done, and so it is difficult to translate helium luminosity limits to stripped helium masses. As an approximate solution, we utilize the Botyánszki et al. (2018) model where they replaced hydrogen with helium in

their simulations, and assumed that the helium mass falls off with luminosity with the same quadratic form as for the stripped hydrogen models (see also Sand et al. 2018). From this we infer a limit of $M_{\text{strip}} \sim 4 \times 10^{-3} M_{\odot}$, although this value should be treated with caution. We note that the recent radiative transfer work of Dessart et al. (2020) produced weak or ambiguous helium lines in their simulated spectra, aside from the stronger He I $\lambda 10830 \text{ \AA}$ line. Thus, our helium limits correspond to the lower end of expectations for helium companion stars in the SD model, but further work is needed to produce robust helium line predictions.

In summary, our limits on stripped hydrogen from the SD scenario are $\sim 2\text{--}3$ orders of magnitude below expectations, setting a strong constraint on this scenario, modulo current model limitations. We further rule out most helium companion star scenarios, although our helium limit of $M_{\text{strip}} \sim 4 \times 10^{-3} M_{\odot}$ does overlap with some predictions, so we cannot completely rule out this channel. Our hydrogen limits are similar to or stronger than the $H\alpha$ recently seen in the fast-declining SNe Ia ASASSN-18tb ($L_{H\alpha} = 2.2 \times 10^{38} \text{ erg s}^{-1}$; Kollmeier et al. 2019), SN 2018cuj ($L_{H\alpha} = 3.8 \times 10^{37} \text{ erg s}^{-1}$; Prieto et al. 2020), and SN 2016jag ($L_{H\alpha} = 1.6\text{--}3.0 \times 10^{38} \text{ erg s}^{-1}$; Elias-Rosa et al. 2021). As an aside, our hydrogen limits also rule out any hydrogen-rich CSM (although the model expectations are less clear here), which may be interacting with the ejecta at this epoch. Outside of the SD scenario, such CSM may plausibly be associated with a giant planet (Soker 2019) or a nondegenerate tertiary star (Thompson 2011; Kushnir et al. 2013; Vallely et al. 2019), which does not seem to be the case for SN 2020nlb.

6. SN 2020nlb Constraints on Circumstellar Interaction from Radio Observations

Radio emission can independently probe the presence of CSM because interaction of the SN ejecta with this CSM accelerates electrons to relativistic energies and amplifies the ambient magnetic field, producing radio synchrotron emission (Chevalier 1982, 1984, 1998). Simple models of radio emission have provided constraints on the CSM environment and progenitor properties for both core-collapse (e.g., Ryder et al. 2004; Soderberg et al. 2006a; Chevalier & Fransson 2006; Weiler et al. 2007; Salas et al. 2013; Bostroem et al. 2019) and Type Ia SNe (Panagia et al. 2006; Chomiuk et al. 2016). Radio emission is yet to be detected from a Type Ia SN, but non-detections have provided stringent constraints on their progenitor scenarios (Chomiuk et al. 2016), particularly for nearby events (Horesh et al. 2012b; Chomiuk et al. 2012; Pérez-Torres et al. 2014; Pellegrino et al. 2020; Lundqvist et al. 2020; Burke et al. 2021).

Below we describe our VLA observations of SN 2020nlb. SN 2017cbv is outside the decl. limit of the VLA, and we are not aware of any radio observations that were associated with this SN.

6.1. Observation

A radio observation of SN 2020nlb was obtained with the Karl G. Jansky Very Large Array (VLA) on 2020 July 7 at 21:49, which is 14.6 days since explosion (derived in Section 2.2). The observation block was 1 hr long, with 37.5 minutes on-source time for SN 2020nlb. Observations were taken in the C band (4–8 GHz) in the B configuration of the

VLA (DDT: 20A-577, PI: S. Sarbadhicary). The observations were obtained in wide-band continuum mode, yielding 4 GHz of bandwidth sampled by 32 spectral windows, each 128 MHz wide sampled by 1 MHz wide channels with two polarizations. We used 3C286 as our flux, delay, and bandpass calibrator, and J1224+2122 as our complex gain calibrator. Data were calibrated with the VLA CASA calibration pipeline (version 5.6.1-8), which iteratively flags corrupted measurements, applies corrections from the online system (e.g., antenna positions), and applies delay, flux density, bandpass, and complex gain calibrations. We then imaged the calibrated visibility data set with `tclean` in CASA. We used multi-term, multifrequency synthesis as our deconvolution algorithm (set with `deconvolver = 'mtmfs'` in `tclean`), which approximates the full 4–8 GHz wide-band spectral structure of the sky brightness distribution as a Taylor-series expansion about a reference frequency (in our case, 6 GHz) in order to reduce frequency-dependent artifacts during deconvolution (Rau & Cornwell 2011). We set `nterms = 2`, which uses the first two Taylor terms to create images of intensity (Stokes-I) and spectral index. We sampled the synthesized beam with 3–4 pixels, and imaged out to $11.2'$ (about 12% sensitivity level of primary beam) to deconvolve any outlying bright sources and mitigate their sidelobes at the primary beam center. Gridding was carried out with the W-projection algorithm (`gridding = wproject`) with 16 w-planes. Images were weighted with the Briggs weighting scheme (`weighting = briggs`) using a robust value of 0 to balance point-source sensitivity with high angular resolution and low sidelobe contamination between sources. The final image has a spatial resolution of $0.9'' \times 0.8''$ (or roughly $79 \times 70 \text{ pc}$), and an rms of about $5 \mu\text{Jy beam}^{-1}$, which is within 25% of the expected thermal noise level of our observation.²⁰

No radio source was detected at the site of SN 2020nlb in the cleaned, deconvolved 6 GHz image at the 3σ level. The flux at the SN location is $6.4 \mu\text{Jy beam}^{-1}$, and the rms noise in a circular region $7''$ across around the SN location is $4.5 \mu\text{Jy beam}^{-1}$. We therefore assume a flux density upper limit of $19.7 \mu\text{Jy beam}^{-1}$, which is equal to the flux density at the SN location plus three times the rms noise. At a distance of 17.9 Mpc, this corresponds to a 6 GHz luminosity of $7.6 \times 10^{24} \text{ erg s}^{-1} \text{ Hz}^{-1}$.

6.2. Analysis

The luminosity upper limit can shed some light on the CSM around SN 2020nlb similar to the methodology in Chomiuk et al. (2012) and Chomiuk et al. (2016). We assume SN 2020nlb was surrounded by the Chevalier (1982) model of a CSM, produced by steady mass loss from the progenitor, i.e., $\rho_{\text{csm}} = \dot{M}/4\pi r^2 v_w$ (where ρ_{csm} is the CSM density in g cm^{-3} , \dot{M} is the mass-loss rate from the progenitor, r is the distance from the progenitor, and v_w is the wind velocity). Assuming a standard SN Ia explosion with 10^{51} erg kinetic energy and $1.4 M_{\odot}$ ejecta mass, we obtain a mass-loss rate upper limit of $\dot{M} < (3.7 - 16.7) \times 10^{-9} M_{\odot} \text{ yr}^{-1}$, assuming $v_w = 10 \text{ km s}^{-1}$. The range of mass-loss rates reflect the uncertainty in the parameter ϵ_B , the fraction of shock energy shared by the amplified magnetic field, with typical values in the range 0.01–0.1 for SNe (Chomiuk et al. 2012). These limits are compared with the mass-loss rate parameter space of SD

²⁰ <https://obs.vla.nrao.edu/ect/>

models, as defined in Chomiuk et al. (2012), in Figure 6. We find that our limits are deep enough to rule out red-giant companions (symbiotic systems), characterized by slow winds of $10\text{--}100\text{ km s}^{-1}$ and mass-loss rates of $10^{-6}\text{--}10^{-8}\text{ }M_{\odot}\text{ yr}^{-1}$ (Seaquist & Taylor 1990). Symbiotic systems have also been ruled out for the majority of SNe Ia based on their radio upper limits (Horesh et al. 2012b; Chomiuk et al. 2012; Pérez-Torres et al. 2014; Chomiuk et al. 2016; Pellegrino et al. 2020; Lundqvist et al. 2020; Burke et al. 2021). Many models involving main-sequence companions however are still allowed within our limits of SN 2020nlb (see colored regions in Figure 6).

7. X-Ray Constraints on CSM

Deep X-ray observations can constrain the density of the circumstellar environment in the region around the supernova, which has inevitably been shaped by any mass loss in the progenitor system prior to explosion. Within $\delta t \lesssim 40$ days of explosion, the X-ray emission in low density environments, such as that expected from SNe Ia, is dominated by inverse Compton scattering of photospheric photons by relativistic electrons accelerated by the SN shock (Chevalier & Fransson 2006). A generalized formalism for the inverse Compton luminosity was developed by Margutti et al. (2012), building off of the work of Chevalier & Fransson (2006), which depends on the bolometric luminosity of the SN ($L_{\text{IC}} \propto L_{\text{bol}}$), the SN ejecta mass (M_{ej}) and explosion energy (E), the density structure of the SN ejecta (ρ_{SN}), the density structure of the CSM (ρ_{CSM}), and the number of electrons and their energy distribution (p and ϵ_e), which is responsible for the upscattering of the optical photons to X-ray energies. Here, we adopt this formalism for determining the X-ray inverse Compton luminosity, using many of the assumptions made in that work, which have been utilized to constrain the low density CSM around several other nearby SNe Ia—most stringently for SN 2011fe (Margutti et al. 2012) and SN 2014J (Margutti et al. 2014), but also SN 2012cg (Shappee et al. 2018), SN 2018oh (Shappee et al. 2019), and SN Iax 2014dt (Stauffer et al. 2021). We also use the bolometric luminosities discussed in Section 4 for our results here.

As in previous work, we assume the outer density of the SN scales as $\rho_{\text{SN}} \propto R^{-n}$ with $n = 10$ (see, e.g., Matzner & McKee 1999, for compact progenitors). The electrons are assumed to be distributed like a power-law distribution dependent on the Lorentz factor (γ), $n_e(\gamma) \propto \gamma^{-p}$ with index $p = 3$; this value is supported by observations of SN Ib/c shocks (e.g., Soderberg et al. 2006b). We assume the fraction of post-shock energy density in relativistic electrons is $\epsilon_e = 0.1$, as other SN shocks have indicated (Chevalier & Fransson 2006); CSM density limits scale as $(\epsilon_e/0.1)^{-2}$ for any variation in this parameter (Margutti et al. 2012). Unlike similar radio constraints on the CSM, X-ray observations do not require any assumptions about magnetic field-related parameters (see dotted lines in Figure 6). As both SN 2017cbv and SN 2020nlb appear to be *normal* SNe Ia we adopt an ejecta mass of $M_{\text{ej}} = 1.4\text{ }M_{\odot}$ and explosion energy of $E = 10^{51}$ erg for each; these are the same values adopted in the X-ray analysis for SN 2011fe and SN 2014J (Margutti et al. 2012, 2014).

We explore two different scenarios for the CSM environment: (1) a constant-density interstellar matter (ISM)-like CSM ($\rho_{\text{CSM}} = \text{constant}$) and (2) a wind-like CSM ($\rho_{\text{CSM}} \propto R^{-2}$). In a simple case, a star that has been losing material at a constant

rate, \dot{M} , with wind velocity, v_w , has a *wind-like* CSM with $\rho_{\text{CSM}} = \dot{M}/(4\pi R^2 v_w)$, and would be a signature of the SD scenario. DD scenarios would have *clean* environments with no CSM or a low density ISM-like CSM (although see discussion below). We do not consider asymmetric or CSM configurations with cavities explicitly here with our observational constraints, although we discuss a wide variety of CSM geometries in the following section.

For an ISM-like medium, and using the Margutti et al. (2012) formalism along with the bolometric luminosities in Section 4, we derive limits of $n_{\text{CSM}} < 35.8\text{ cm}^{-3}$ and $< 65\text{ cm}^{-3}$ for SN 2017cbv and SN 2020nlb, respectively. Given the epoch that the X-ray data were taken, they probe radii of $R_{\text{ISM}} = 1.4 \times 10^{16}$ and $1.2 \times 10^{16}\text{ cm}$, respectively, for SN 2017cbv and SN 2020nlb. These constraints are within an order of magnitude of those from SN 2011fe ($< 166\text{ cm}^{-3}$) and SN 2014J ($< 3.5\text{ cm}^{-3}$).

Similarly, for a wind-like medium and fiducial wind velocity of $v_w = 100\text{ km s}^{-1}$, we constrain the progenitor mass-loss rate to be $\dot{M} < 7.2 \times 10^{-9}$ and $\dot{M} < 9.7 \times 10^{-9}\text{ }M_{\odot}\text{ yr}^{-1}$ for SN 2017cbv and SN 2020nlb, respectively. At the epoch of the Chandra observations, these correspond to radii of 1.9×10^{16} and $1.6 \times 10^{16}\text{ cm}$ for the two SNe. These constraints are weaker than those of SN 2011fe ($\dot{M} \lesssim 2 \times 10^{-9}\text{ }M_{\odot}\text{ yr}^{-1}$) and SN 2014J ($\dot{M} \lesssim 1 \times 10^{-9}\text{ }M_{\odot}\text{ yr}^{-1}$), but are the same order of magnitude.

In Figure 5, we plot the time evolution of the expected inverse Compton X-ray emission corresponding to the limits obtained for both the ISM and wind-like CSM scenarios described above, alongside our Chandra X-ray limits. In the following section we discuss the physical implications for the SN progenitor systems that these constraints provide.

8. Discussion

We have presented deep Chandra X-ray observations of SN 2017cbv and SN 2020nlb around optical maximum light in order to constrain the environment around these SN Ia explosions. In addition to this data, we have presented VLA radio observations and a deep nebular spectrum of SN 2020nlb to further constrain the progenitor of this nearby SN. The X-ray observations double the sample of normal SNe Ia with such deep limits, and regardless of the assumed circumburst density profile, they imply a *clean* environment at distances of $R \lesssim 10^{16}\text{ cm}$ from the explosion. We focus our discussion on the constraints that these data provide on the progenitor system in this section.

8.1. SD Scenarios with Near-steady Mass Loss

In the SD scenario, where a white dwarf near the Chandrasekhar mass is accreting from a companion star (at a rate of $\dot{M}_{\text{acc}} \gtrsim 3 \times 10^{-7}\text{ }M_{\odot}\text{ yr}^{-1}$ for steady hydrogen burning; Shen & Bildsten 2007), material can be lost to the surrounding environment via donor star winds, nonconservative mass transfer through Roche lobe overflow, or even winds from the accreting white dwarf itself—inverse Compton X-ray emission around maximum light can probe all of these scenarios.

Symbiotic binary systems are plausible SN Ia progenitor systems, where the white dwarf accretes wind material from an evolved giant star. Mass-loss rates range from $\dot{M} \approx 5 \times 10^{-9}$ to $5 \times 10^{-6}\text{ }M_{\odot}\text{ yr}^{-1}$ with wind velocities $v_w \lesssim 100\text{ km s}^{-1}$ (e.g.,

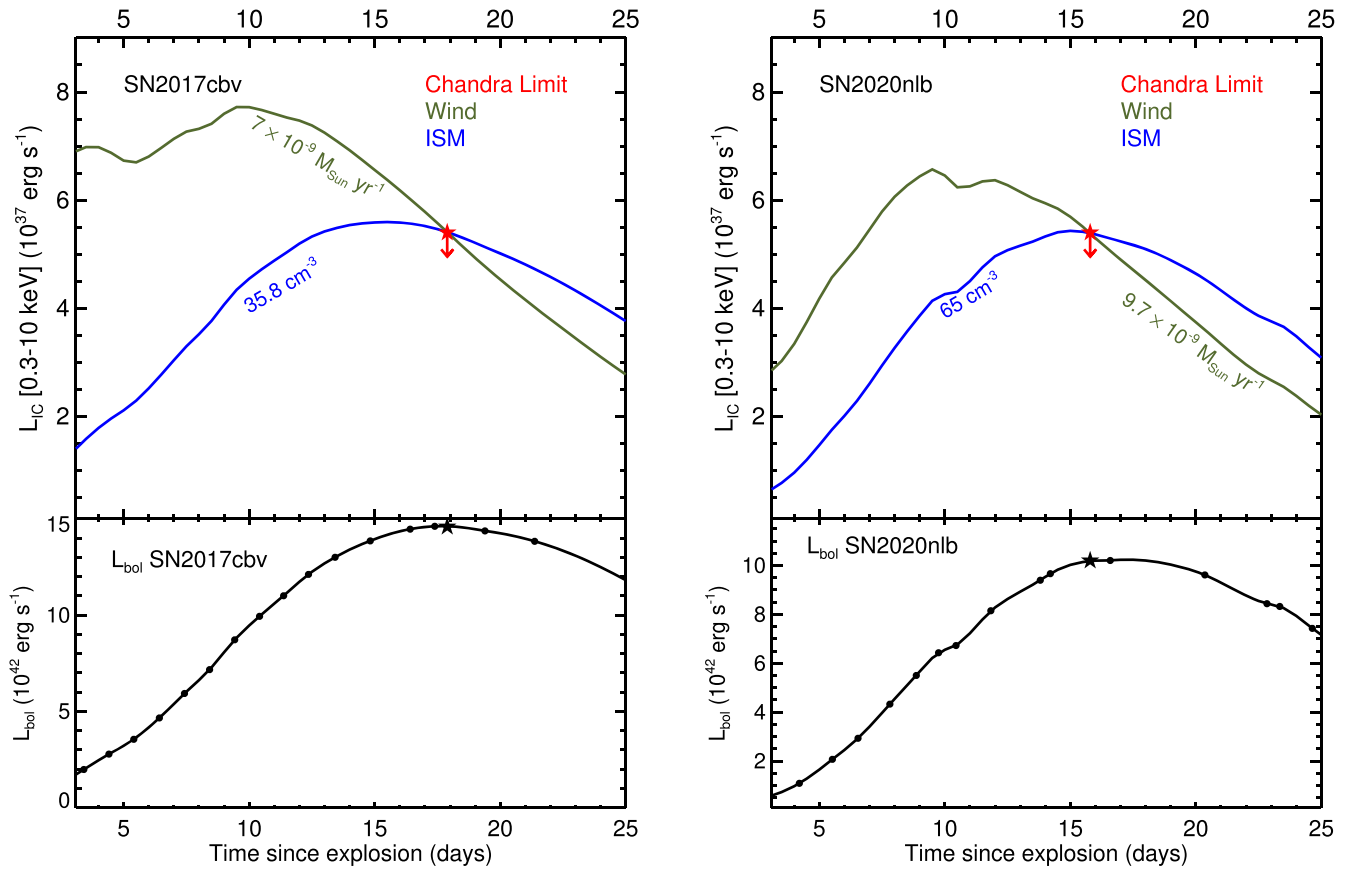


Figure 5. Top panels—expected maximum inverse Compton X-ray luminosity in the case of wind (green, with an assumed $v_w = 100 \text{ km s}^{-1}$) and ISM-like (blue) environments for SN 2017cbv (left) and SN 2020nlb (right), based on the Chandra X-ray limits (red upper limits) for each. Bottom panels—bolometric light curves for SN 2017cbv (data from Wang et al. 2020) and SN 2020nlb (this work). The interpolated bolometric luminosity of the SN at the epoch of the Chandra observations is marked with a star symbol.

Sequist & Taylor 1990; Patat et al. 2011; Chen et al. 2011, see also discussion in Meng & Han 2016), as illustrated in the appropriate block of Figure 6. Our new X-ray observations (complemented by our radio observations of SN 2020nlb) can rule out all plausible symbiotic systems. While the sample size is still small, combining the current X-ray results with those from SN 2014J and SN 2011fe suggest that symbiotic-like CSM is uncommon around SN Ia systems. Using their much larger sample of SNe Ia with radio observations, Chomiuk et al. (2016) similarly conclude that $\lesssim 10\%$ of SNe Ia are in symbiotic systems.

It is also possible that lower mass, nondegenerate companions (main-sequence, subgiant, or helium stars) are influencing the CSM environment through nonconservative mass transfer. Here, the nondegenerate secondary star fills its Roche lobe and some material is lost to the environment at the outer Lagrange point. We estimate the typical velocity of this lost and ejected material to be a few hundred kilometers per second, the same order as the orbital velocity of the white dwarf, with an upper limit of $\sim 600 \text{ km s}^{-1}$, corresponding to the limit seen in stable nuclear burning white dwarfs (Deufel et al. 1999). The fraction of material lost is unknown, but is often assumed to be $\epsilon_{\text{loss}} \approx 1\%$, thus leading to the expected mass-loss range of $\dot{M} \approx 0.3\text{--}3 \times 10^{-8} M_{\odot} \text{ yr}^{-1}$ shown in Figure 2. Our new observations of SN 2017cbv and SN 2020nlb cut into this region of parameter space (see Figure 6), but do not completely rule out this *Lagrangian losses* scenario. Indeed, if the real fraction of material lost at the outer Lagrange points is

significantly less than $\epsilon_{\text{loss}} \approx 1\%$, then this scenario would remain plausible for all X-ray constraints published thus far, and it is likely that a next-generation X-ray mission is necessary to fully rule out this scenario.

If the accretion rate from a nondegenerate companion is high enough, optically thick winds from the white dwarf are expected to develop, which happens around a critical value of $\dot{M}_{\text{acc}} \sim 7 \times 10^{-7} M_{\odot} \text{ yr}^{-1}$ depending on the hydrogen mass fraction and white dwarf mass (Hachisu et al. 1999; Han & Podsiadlowski 2004; Shen & Bildsten 2007), leading to the range of allowed mass losses associated with the *accretion winds* scenario in Figure 6 (although see the recent models of Dragulin & Hoefflich 2016), which suggest a low density cavity near the progenitor system that would lead to weaker limits). The associated white dwarf wind velocities can be up to a few thousand kilometers per second (Hachisu et al. 1999), similar to the outflows seen in X-ray luminous, nuclear burning white dwarfs (Cowley et al. 1998). Our X-ray constraints on SN 2017cbv and SN 2020nlb largely rule out this SD progenitor scenario (as have the X-ray observations of SN 2011fe and SN 2014J), although a small region of the allowed parameter space (at high velocities, $\gtrsim 1000 \text{ km s}^{-1}$, and low mass-loss rates, $\sim 10^{-7} M_{\odot} \text{ yr}^{-1}$) are still viable.

8.2. Non-steady Mass Loss in the SD Scenario

Our X-ray analysis is most sensitive to progenitor scenarios with continuous mass loss up until the point of the SN explosion, although there are many instances where this may

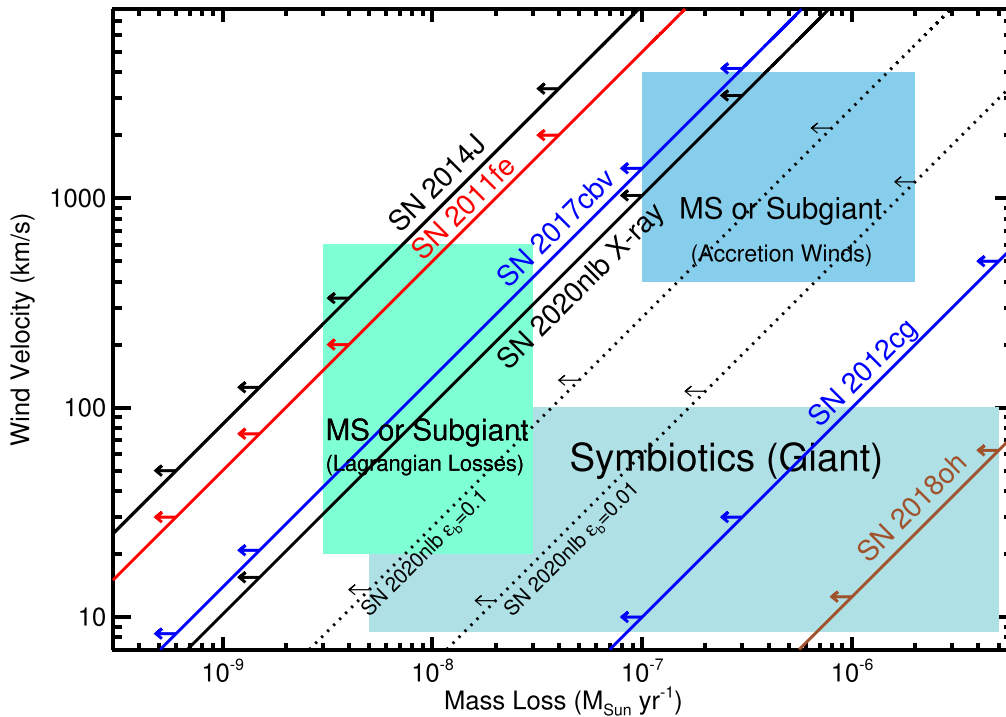


Figure 6. X-ray constraints on a wind-like CSM for SN 2017cbv (blue line) and SN 2020nlb (solid black line) with respect to other prominent results in the literature. Regions of parameter space not ruled out are toward the upper left of the plot, in the direction of the arrows. The color blocked regions represent areas of parameter space where plausible SN Ia progenitors and their expected CSM would inhabit, which we discuss further in Section 8. Limits obtained for other prominent SNe Ia include SN 2011fe (Margutti et al. 2012), SN 2014J (Margutti et al. 2014), SN 2012cg (Shappee et al. 2018) and SN 2018oh (Shappee et al. 2019). The data from Russell & Immler (2012), as seen in Figure 3, all lie to the right of SN 2012cg in this plot. We also plot our radio CSM constraints for SN 2020nlb (dotted lines; Section 6) assuming $\epsilon_b = 0.01$ and 0.1 for the fraction of shock energy shared by the amplified magnetic field; these observations alone rule out portions of the parameter space occupied by symbiotics and accretion winds.

not be the case, even within the SD scenario. If there is noncontinuous mass loss in the time period just preceding explosion, our observations would be insensitive to any material inside or outside of $R \approx 10^{16}$ cm.

Recurrent nova systems are plausible SN Ia progenitors, with a high mass white dwarf ($>1.3 M_\odot$) accreting at 10^{-8} – $10^{-7} M_\odot \text{ yr}^{-1}$ (Livio & Truran 1992; Yaron et al. 2005), and experiencing repeated nova explosions due to unsteady hydrogen burning. The recurrent nova system RS Oph is a prominent example of this class of objects (Patat et al. 2011), where the white dwarf increases in mass with time (Hachisu & Kato 2001) unlike in classical nova systems. SN Ia PTF11kx, for instance, showed clear evidence of nova shells in multi-epoch high resolution spectroscopy and is suggested to have a recurrent nova progenitor system (Dilday et al. 2012), as have other SNe Ia with signs of interaction (e.g., SN 2002ic; Wood-Vasey & Sokoloski 2006).

The CSM for recurrent nova systems is expected to be complex, and may include relatively high density nova shells, with nearly evacuated regions or wind material from the donating star in between; it is also possible there is a central cavity with no material as well (see discussion in Dimitriadis et al. 2014; Darnley et al. 2019). The exact geometry of the CSM will depend on the time since the last nova outburst, and the outbursting history. In this scenario, we would need to be very lucky to perform our X-ray observations at the time when the blast wave is interacting with a nova shell, as in between the CSM density would be $<10^{-2} \text{ cm}^{-3}$ (e.g., see Figure 9 in Dimitriadis et al. 2014), far below our constraints of $\lesssim 36$ – 65 cm^{-3} . In any case, neither SN 2017cbv nor SN 2020nlb show any signs of interaction in their spectra

(see the high resolution optical spectroscopic sequence of Ferretti et al. 2017, in particular).

Other scenarios where the mass loss stops prior to explosion would also yield non-detections in our X-ray data if the material is all at $\gtrsim 10^{16}$ cm, or if the delay between the cessation of mass loss and explosion were $t \gtrsim 30 \times (v_w/100 \text{ km s}^{-1})^{-1} \text{ yr}$. One model where this can occur is the so-called spin-up/spin-down scenario, where the accreting white dwarf gains enough angular momentum during the accretion process that it will not explode at the Chandrasekhar mass, and must spin down before it explodes (Di Stefano et al. 2011; Justham 2011). Another scenario with potentially long delays between mass loss and the explosion is the core degenerate scenario, where the white dwarf merges with the core of an asymptotic giant branch star at the end of the common envelope phase (Kashi & Soker 2011; Ilkov & Soker 2012); here again, the rapid rotation of the white dwarf may prevent it from exploding immediately. In both cases, the key unknown is the delay time between the completion of mass transfer and explosion, and is difficult to assess because the physical mechanism of the spin down is not certain although calculations have suggested delays ranging from $\lesssim 10^5$ to $\gtrsim 10^9$ yr (Lindblom et al. 1999; Yoon & Langer 2005; Ilkov & Soker 2012; Hachisu et al. 2012); if one of these SD scenarios were responsible for a sizable proportion of SNe Ia, it would be difficult to discern with X-ray observations.

8.3. White Dwarf–White Dwarf Progenitors

In the DD scenario, two white dwarfs coalesce and lead to the final SN Ia explosion. The general prediction for this

scenario is for a *clean* circumbinary environment on scales greater than $R \gtrsim 10^{14}$ cm (Fryer et al. 2010; Shen et al. 2012; Raskin & Kasen 2013), similar to the ISM. Despite this, there are several ways in which a white dwarf–white dwarf merger can enrich the circumbinary environment. We briefly discuss these scenarios in the context of our X-ray limits at $\sim 10^{16}$ cm.

One feature of white dwarf–white dwarf merger calculations is the tidal stripping and ejection of mass just prior to coalescence, consisting of 10^{-4} – $10^{-2} M_{\odot}$ of material moving at ~ 2000 km s $^{-1}$ in the equatorial region (Dan et al. 2011; Raskin & Kasen 2013), equivalent to an effective mass-loss rate of $\dot{M} \approx 10^{-2}$ – $10^{-5} M_{\odot}$ yr $^{-1}$ (Raskin & Kasen 2013). If this CSM, produced during the coalescence, is at appropriate radii at explosion ($\sim 10^{16}$ cm), then it could lead to detectable inverse Compton emission in the X-ray regime. The key parameter is the time between coalescence (and tidal tail ejection), and the SN explosion, which needs to be $\sim 10^8$ s to reach the radii that X-ray observations are sensitive to. Our observations rule out such delays between coalescence and explosion, although we cannot comment on explosions that occur on a dynamical ($\sim 10^2$ – 10^3 s) or viscous timescale ($\sim 10^4$ – 10^8 s); longer timescales ($\gg 10^8$ s) are also not excluded by our data.

One variant of the DD scenario, the *double detonation* model, posits a progenitor configuration with a carbon-oxygen white dwarf accreting from a helium white dwarf companion (e.g., Nomoto 1982; Livne 1990; Woosley & Weaver 1994). In certain scenarios, hydrogen-rich material on the surface of the helium white dwarf accretes onto the carbon-oxygen white dwarf until convective hydrogen burning is ignited (akin to a classical nova), causing the envelope on the carbon-oxygen white dwarf to expand and overflow its Roche radius, ejecting material at ~ 1500 km s $^{-1}$ (Shen et al. 2013), typically ≈ 3 – $6 \times 10^{-5} M_{\odot}$. Unfortunately, such a shell ejection must occur ~ 2 – 3 yr prior to the final explosion in order for it to be detectable by our X-ray observations (assuming ~ 1500 km s $^{-1}$ ejected velocity), which are probing $\sim 10^{16}$ cm; the simulations presented by Shen et al. (2013) indicate that the timescales for these nova-like shell ejections are more like hundreds to thousands of years prior to explosion, depending on the details of the white dwarf progenitors. Thus, while our X-ray observations can rule out short *ejection to explosion* delay times, they are not a stringent test of this double detonation prediction.

Other DD scenarios with some CSM are also plausible, including mass outflows during rapid accretion events (e.g., Guillochon et al. 2010; Dan et al. 2011) and disk winds from white dwarf mergers that do not promptly detonate (Ji et al. 2013), although these both require specific timing between the mass ejection and eventual explosion of roughly a few years to have material at $\sim 10^{16}$ cm where we have X-ray constraints. Our observations of SN 2017cbv and SN 2020nlb (along with SN 2011fe and SN 2014J) largely rule out these ejection to explosion timescales.

9. Summary and Future Outlook

In this work, we have presented deep Chandra X-ray observations of two nearby Type Ia SNe around maximum light, SN 2017cbv and SN 2020nlb. X-ray observations of SNe Ia in the time period around maximum light are sensitive to inverse Compton emission, which is caused by interaction between the SN blast wave and accelerated particles in the

CSM surrounding the explosion. As this CSM was shaped by the mass-loss history of the progenitor star system leading up to the explosion, X-ray observations are a sensitive probe of the pre-explosion SN environment, and ultimately the progenitor system itself. The analysis of deep X-ray data for two additional, normal SNe Ia doubles the sample studied in this way, adding to the groundbreaking work on SN 2011fe (Margutti et al. 2012) and SN 2014J (Margutti et al. 2014).

The Chandra data lead to X-ray luminosity limits of $L_X \lesssim 5.4 \times 10^{37}$ and $\lesssim 5.4 \times 10^{37}$ erg s $^{-1}$ (0.3–10 keV) at 17.9 and 15.8 days after explosion for SN 2017cbv and SN 2020nlb, respectively. Using the inverse Compton formalism of Margutti et al. (2012) (see also Chevalier & Fransson 2006), which is appropriate for SNe Ia in low density environments in the weeks after explosion, this corresponds to $n_{\text{CSM}} < 36$ and < 65 cm $^{-3}$ at a radius of $R = 1.4 \times 10^{16}$ and 1.2×10^{16} cm for the two SNe, assuming a constant-density ISM-like circumstellar medium. If we assume a wind-like medium (where $\rho_{\text{CSM}} = \dot{M}/(4\pi R^2 v_w)$), we obtain mass-loss limits of $\dot{M} < 7.2 \times 10^{-9}$ and $< 9.7 \times 10^{-9} M_{\odot}$ yr $^{-1}$ for a fiducial wind velocity of $v_w = 100$ km s $^{-1}$ at a radius of $R = 1.9 \times 10^{16}$ and 1.6×10^{16} cm. These limits rule out several prospects for the SD scenario, including all symbiotic progenitor star systems, as well as large portions of the parameter space associated with mass loss at the outer Lagrange point and white dwarf accretion winds. It is difficult for current X-ray observations to rule out DD scenarios as the expectation is for a generally *clean* environment around the SN, unless the timing between the ejection of tidal tails (or other material) is properly timed with the subsequent explosion such that there is significant material at $\sim 10^{16}$ cm (which the X-ray observations probe).

In addition to our X-ray analysis, we have also presented other complementary constraints on the progenitor system of SN 2020nlb, and complementary constraints have already been published for SN 2017cbv. Using a nebular phase spectrum of SN 2020nlb, we set strong constraints on any swept up hydrogen or helium from a nondegenerate companion star in the SD scenario, obtaining limits that were ~ 2 – 3 orders of magnitude below expectations for that channel; our data would have also detected the H α features recently observed in three fast-declining SN Ia (Kollmeier et al. 2019; Prieto et al. 2020; Elias-Rosa et al. 2021). We also obtained VLA data of SN 2020nlb around 15 days after the explosion, and the non-detection allowed us to rule out most plausible symbiotic progenitor systems, in agreement with the X-ray data. These complementary constraints on the progenitor of SN 2020nlb stand alongside the other SN studied in X-rays in this paper, SN 2017cbv. Although SN 2017cbv had an early, blue light-curve bump that may have signalled interaction with a nondegenerate companion star (Hosseinzadeh et al. 2017a), neither nebular spectroscopy (Sand et al. 2018) nor the X-ray constraints in the current work yield any further hints of the SD scenario.

Future directions for X-ray constraints on the CSM around nearby SNe Ia are clear. Even with the current study, only four nearby SNe Ia have been studied to sufficient depths to rule out some standard SD scenarios that predict winds or accretion losses. X-ray CSM constraints on a statistical sample are necessary to make population-level statements about the SN Ia progenitor system and its diversity, and it is vital to have observations spanning the range of SN Ia properties (including

luminosity, light-curve parameters, and subtype). We also advocate for multiple observational probes of the SN Ia progenitor system be made for each nearby SN Ia (e.g., high cadence early light curves to search for *bumps*, late-time search for narrow hydrogen and helium lines, radio CSM constraints, etc.), as each technique has its own strengths, dependence on modeling, and systematic uncertainties. By combining probes for the few SNe Ia that are near enough, progress can be made.

The scientific results reported in this article are based to a significant degree on observations made by the Chandra X-ray Observatory (Obs ID: 20055, 23314, 23315). We thank H. Tananbaum and the entire Chandra team for making the X-ray observations possible.

Support for this work was provided by the National Aeronautics and Space Administration through Chandra Award Number DDO-21119X issued by the Chandra X-ray Center, which is operated by the Smithsonian Astrophysical Observatory for and on behalf of the National Aeronautics Space Administration under contract NAS8-03060. This work makes use of observations from the Las Cumbres Observatory network. The LCO team is supported by NSF grants AST-1911225 and AST-1911151 and NASA Swift grant 80NSSC19K1639. Research by S.V. is supported by NSF grants AST-1813176 and AST-2008108. Time domain research by D.J.S. is also supported by NSF grants AST-1821987, 1813466, 1908972, and 2108032, and by the Heising-Simons Foundation under grant No. 2020-1864. S.K. S. and L.C. are supported by NSF grant AST-1907790 and the Packard Foundation. L.G. acknowledges financial support from the Spanish Ministry of Science, Innovation and Universities (MICIU) under the 2019 Ramón y Cajal program RYC2019-027683 and from the Spanish MICIU project PID2020-115253GA-I00. L.W. is sponsored (in part) by the Chinese Academy of Sciences (CAS) through a grant to the CAS South America Center for Astronomy (CASSACA) in Santiago, Chile.




Observations reported here were obtained at the MMT Observatory, a joint facility of the University of Arizona and the Smithsonian Institution. The National Radio Astronomy Observatory is a facility of the National Science Foundation operated under cooperative agreement by Associated Universities, Inc.


















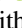
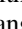
We are grateful to C. Burns for his help with the SNooPy software package.

Facilities: CXO (ACIS), Las Cumbres Observatory (Sinistro), FTN (FLOYDS), MMT (Blue Channel spectrograph), Swift (UVOT), VLA.

Software: astropy (Astropy Collaboration et al. 2013; Astropy Collaboration et al. 2018), The IDL Astronomy User's Library (Landsman 1993), CIAO (Fruscione et al. 2006), Supernova Identification software package (SNIID; Blondin & Tonry 2007), Astrometrica (Raab 2012), SNooPy (Burns et al. 2011, 2014), HEASoft (NASA High Energy Astrophysics Science Archive Research Center (HEASARC) 2014), lcogtsnpipe (Valenti et al. 2016), DoPHOT (Schechter et al. 1993).

ORCID iDs

D. J. Sand  <https://orcid.org/0000-0003-4102-380X>
S. K. Sarbadhicary  <https://orcid.org/0000-0002-4781-7291>
C. Pellegrino  <https://orcid.org/0000-0002-7472-1279>

K. Misra  <https://orcid.org/0000-0003-1637-267X>
R. Dastidar  <https://orcid.org/0000-0001-6191-7160>
P. J. Brown  <https://orcid.org/0000-0001-6272-5507>
S. Valenti  <https://orcid.org/0000-0001-8818-0795>
Jonathan J. Swift  <https://orcid.org/0000-0002-9486-818X>
J. E. Andrews  <https://orcid.org/0000-0003-0123-0062>
K. A. Bostroem  <https://orcid.org/0000-0002-4924-444X>
J. Burke  <https://orcid.org/0000-0003-0035-6659>
L. Chomiuk  <https://orcid.org/0000-0002-8400-3705>
Y. Dong  <https://orcid.org/0000-0001-8818-0795>
L. Galbany  <https://orcid.org/0000-0002-1296-6887>
D. Hiramatsu  <https://orcid.org/0000-0002-1125-9187>
D. A. Howell  <https://orcid.org/0000-0003-4253-656X>
E. Y. Hsiao  <https://orcid.org/0000-0003-1039-2928>
D. Janzen  <https://orcid.org/0000-0003-0549-3281>
J. E. Jencson  <https://orcid.org/0000-0001-5754-4007>
M. J. Lundquist  <https://orcid.org/0000-0001-9589-3793>
C. McCully  <https://orcid.org/0000-0001-5807-7893>
D. Reichart  <https://orcid.org/0000-0002-5060-3673>
Nathan Smith  <https://orcid.org/0000-0001-5510-2424>
Lingzhi Wang  <https://orcid.org/0000-0002-1094-3817>
S. Wyatt  <https://orcid.org/0000-0003-2732-4956>

References

- Astropy Collaboration, Price-Whelan, A. M., Sipőcz, B. M., et al. 2018, *AJ*, **156**, 123
- Astropy Collaboration, Robitaille, T. P., Tollerud, E. J., et al. 2013, *A&A*, **558**, A33
- Bellm, E. C., Kulkarni, S. R., Graham, M. J., et al. 2019, *PASP*, **131**, 018002
- Bianco, F. B., Howell, D. A., Sullivan, M., et al. 2011, *ApJ*, **741**, 20
- Blondin, S., Dessart, L., Hillier, D. J., & Khokhlov, A. M. 2013, *MNRAS*, **429**, 2127
- Blondin, S., Dessart, L., Hillier, D. J., & Khokhlov, A. M. 2017, *MNRAS*, **470**, 157
- Blondin, S., Matheson, T., Kirshner, R. P., et al. 2012, *AJ*, **143**, 126
- Blondin, S., & Tonry, J. L. 2007, *ApJ*, **666**, 1024
- Boehner, P., Plewa, T., & Langer, N. 2017, *MNRAS*, **465**, 2060
- Bostroem, K. A., Valenti, S., Horesh, A., et al. 2019, *MNRAS*, **485**, 5120
- Botyánszki, J., Kasen, D., & Plewa, T. 2018, *ApJL*, **852**, L6
- Branch, D., Dang, L. C., Hall, N., et al. 2006, *PASP*, **118**, 560
- Breeveld, A. A., Curran, P. A., Hooversten, E. A., et al. 2010, *MNRAS*, **406**, 1687
- Brown, P. J., Breeveld, A. A., Holland, S., Kuin, P., & Pritchard, T. 2014, *Ap&SS*, **354**, 89
- Brown, P. J., Dawson, K. S., Harris, D. W., et al. 2012, *ApJ*, **749**, 18
- Brown, T. M., Baliber, N., Bianco, F. B., et al. 2013, *PASP*, **125**, 1031
- Burke, J., Howell, D. A., Sarbadhicary, S. K., et al. 2021, *ApJ*, **919**, 142
- Burns, C. R., Ashall, C., Contreras, C., et al. 2020, *ApJ*, **895**, 118
- Burns, C. R., Stritzinger, M., Phillips, M. M., et al. 2011, *AJ*, **141**, 19
- Burns, C. R., Stritzinger, M., Phillips, M. M., et al. 2014, *ApJ*, **789**, 32
- Burrows, D. N., Hill, J. E., Nousek, J. A., et al. 2005, *SSRv*, **120**, 165
- Cao, Y., Kulkarni, S. R., Howell, D. A., et al. 2015, *Natur*, **521**, 328
- Chen, X., Han, Z., & Tout, C. A. 2011, *ApJL*, **735**, L31
- Chevalier, R. A. 1982, *ApJ*, **259**, 302
- Chevalier, R. A. 1984, *ApJL*, **285**, L63
- Chevalier, R. A. 1998, *ApJ*, **499**, 810
- Chevalier, R. A., & Fransson, C. 2006, *ApJ*, **651**, 381
- Chomiuk, L., Soderberg, A. M., Chevalier, R. A., et al. 2016, *ApJ*, **821**, 119
- Chomiuk, L., Soderberg, A. M., Moe, M., et al. 2012, *ApJ*, **750**, 164
- Cowley, A. P., Schmidtke, P. C., Crampton, D., & Hutchings, J. B. 1998, *ApJ*, **504**, 854
- Dan, M., Rosswog, S., Guillochon, J., & Ramirez-Ruiz, E. 2011, *ApJ*, **737**, 89
- Damley, M. J., Hounsell, R., O'Brien, T. J., et al. 2019, *Natur*, **565**, 460
- Dessart, L., Leonard, D. C., & Prieto, J. L. 2020, *A&A*, **638**, A80
- Deufel, B., Barwig, H., Šimić, D., Wolf, S., & Drory, N. 1999, *A&A*, **343**, 455
- Di Stefano, R., Voss, R., & Claeys, J. S. W. 2011, *ApJL*, **738**, L1
- Dilday, B., Howell, D. A., Cenko, S. B., et al. 2012, *Sci*, **337**, 942
- Dimitriadis, G., Chiotellis, A., & Vink, J. 2014, *MNRAS*, **443**, 1370
- Dimitriadis, G., Foley, R. J., Rest, A., et al. 2019, *ApJL*, **870**, L1
- Dimitriadis, G., Rojas-Bravo, C., Kilpatrick, C. D., et al. 2019, *ApJL*, **870**, L14

- Dragulin, P., & Hoefflich, P. 2016, *ApJ*, **818**, 26
- Elias-Rosa, N., Chen, P., Benetti, S., et al. 2021, *A&A*, **652**, A115
- Ferretti, R., Amanullah, R., Bulla, M., et al. 2017, *ApJL*, **851**, L43
- Flewelling, H. A., Magnier, E. A., Chambers, K. C., et al. 2020, *ApJS*, **251**, 7
- Folatelli, G., Morrell, N., Phillips, M. M., et al. 2013, *ApJ*, **773**, 53
- Fruscione, A., McDowell, J. C., Allen, G. E., et al. 2006, *Proc. SPIE*, **6270**, 62701V
- Fryer, C. L., Ruiter, A. J., Belczynski, K., et al. 2010, *ApJ*, **725**, 296
- Ganeshalingam, M., Li, W., & Filippenko, A. V. 2011, *MNRAS*, **416**, 2607
- Gehrels, N., Chincarini, G., Giommi, P., et al. 2004a, *ApJ*, **611**, 1005
- Gehrels, N., Chincarini, G., Giommi, P., et al. 2004b, *ApJ*, **611**, 1005
- Graham, M. L., et al. 2017, *MNRAS*, **472**, 3437
- Guillochon, J., Dan, M., Ramirez-Ruiz, E., & Rosswog, S. 2010, *ApJL*, **709**, L64
- Hachisu, I., & Kato, M. 2001, *ApJ*, **558**, 323
- Hachisu, I., Kato, M., & Nomoto, K. 1999, *ApJ*, **522**, 487
- Hachisu, I., Kato, M., Saio, H., & Nomoto, K. 2012, *ApJ*, **744**, 69
- Han, Z., & Podsiadlowski, P. 2004, *MNRAS*, **350**, 1301
- Hayden, B. T., Garnavich, P. M., Kasen, D., et al. 2010, *ApJ*, **722**, 1691
- Holmbo, S., Stritzinger, M. D., Shappee, B. J., et al. 2019, *A&A*, **627**, A174
- Horeh, A., Kulkarni, S. R., Fox, D. B., et al. 2012a, *ApJ*, **746**, 21
- Horeh, A., Kulkarni, S. R., Fox, D. B., et al. 2012b, *ApJ*, **746**, 21
- Hosseinzadeh, G., Howell, D. A., Sand, D., et al. 2017b, *ATel*, **10164**, 1
- Hosseinzadeh, G., Sand, D. J., Valenti, S., et al. 2017a, *ApJL*, **845**, L11
- Hoyt, T. J., Beaton, R. L., Freedman, W. L., et al. 2021, *ApJ*, **915**, 34
- Hsiao, E. Y., Conley, A., Howell, D. A., et al. 2007, *ApJ*, **663**, 1187
- Iben, I., Jr., & Tutukov, A. V. 1984, *ApJS*, **54**, 335
- Ilkov, M., & Soker, N. 2012, *MNRAS*, **419**, 1695
- Jha, S. W., Maguire, K., & Sullivan, W. 2019, *NatAs*, **3**, 706
- Ji, S., Fisher, R. T., García-Berro, E., et al. 2013, *ApJ*, **773**, 136
- Justham, S. 2011, *ApJL*, **730**, L34
- Kalberla, P. M. W., Burton, W. B., Hartmann, D., et al. 2005, *A&A*, **440**, 775
- Kasen, D. 2010, *ApJ*, **708**, 1025
- Kashi, A., & Soker, N. 2011, *MNRAS*, **417**, 1466
- Kollmeier, J. A., Chen, P., Dong, S., et al. 2019, *MNRAS*, **486**, 3041
- Kushnir, D., Katz, B., Dong, S., Livne, E., & Fernández, R. 2013, *ApJL*, **778**, L37
- Landsman, W. B. 1993, in ASP Conf. Ser. 52, Astronomical Data Analysis Software and Systems II, ed. R. J. Hanisch, R. J. V. Brissenden, & J. Barnes (San Francisco, CA: ASP), 246
- Leonard, D. C. 2007, *ApJ*, **670**, 1275
- Li, W., Wang, X., Vinkó, J., et al. 2019, *ApJ*, **870**, 12
- Lindblom, L., Mendell, G., & Owen, B. J. 1999, *PhRvD*, **60**, 064006
- Liu, Z. W., Pakmor, R., Röpke, F. K., et al. 2012, *A&A*, **548**, A2
- Liu, Z.-W., Pakmor, R., Seitenzahl, I. R., et al. 2013, *ApJ*, **774**, 37
- Livio, M., & Truran, J. W. 1992, *ApJ*, **389**, 695
- Livne, E. 1990, *ApJL*, **354**, L53
- Lundqvist, P., Kundu, E., Pérez-Torres, M. A., et al. 2020, *ApJ*, **890**, 159
- Lundqvist, P., Mattila, S., Sollerman, J., et al. 2013, *MNRAS*, **435**, 329
- Lundqvist, P., Nyholm, A., Taddia, F., et al. 2015, *A&A*, **577**, A39
- Maguire, K., Taubenberger, S., Sullivan, M., & Mazzali, P. A. 2016, *MNRAS*, **457**, 3254
- Margutti, R., Parrent, J., Kamble, A., et al. 2014, *ApJ*, **790**, 52
- Margutti, R., Soderberg, A. M., Chomiuk, L., et al. 2012, *ApJ*, **751**, 134
- Marietta, E., Burrows, A., & Fryxell, B. 2000, *ApJS*, **128**, 615
- Marion, G. H., Brown, P. J., Vinkó, J., et al. 2016, *ApJ*, **820**, 92
- Mattila, S., Lundqvist, P., Sollerman, J., et al. 2005, *A&A*, **443**, 649
- Matzner, C. D., & McKee, C. F. 1999, *ApJ*, **510**, 379
- Mei, S., Blakeslee, J. P., Côté, P., et al. 2007, *ApJ*, **655**, 144
- Meng, X., & Han, Z. 2016, *A&A*, **588**, A88
- Miller, A. A., Cao, Y., Piro, A. L., et al. 2018, *ApJ*, **852**, 100
- Miller, A. A., Magee, M. R., Polin, A., et al. 2020, *ApJ*, **898**, 56
- NASA High Energy Astrophysics Science Archive Research Center (HEASARC) 2014, HEASoft: Unified Release of FTOOLS and XANADU, Astrophysics Source Code Library, ascl:1408.004
- Nomoto, K. 1982, *ApJ*, **253**, 798
- Nomoto, K., Thielemann, F. K., & Yokoi, K. 1984, *ApJ*, **286**, 644
- Olling, R. P., Mushotzky, R., Shaya, E. J., et al. 2015, *Natur*, **521**, 332
- Pan, K.-C., Ricker, P. M., & Taam, R. E. 2010, *ApJ*, **715**, 78
- Pan, K.-C., Ricker, P. M., & Taam, R. E. 2012, *ApJ*, **750**, 151
- Panagia, N., Van Dyk, S. D., Weiler, K. W., et al. 2006, *ApJ*, **646**, 369
- Pastorello, A., Mazzali, P. A., Pignata, G., et al. 2007, *MNRAS*, **377**, 1531
- Patat, F., Chugai, N. N., Podsiadlowski, P., et al. 2011, *A&A*, **530**, A63
- Pellegrino, C., Howell, D. A., Sarbadhicary, S. K., et al. 2020, *ApJ*, **897**, 159
- Pereira, R., Thomas, R. C., Aldering, G., et al. 2013, *A&A*, **554**, A27
- Pérez-Torres, M. A., Lundqvist, P., Beswick, R. J., et al. 2014, *ApJ*, **792**, 38
- Phillips, M. M., Lira, P., Suntzeff, N. B., et al. 1999, *AJ*, **118**, 1766
- Piro, A. L., & Nakar, E. 2014, *ApJ*, **784**, 85
- Prieto, J. L., Chen, P., Dong, S., et al. 2020, *ApJ*, **889**, 100
- Raah, H. 2012, Astrometrica: Astrometric Data Reduction of CCD images, Astrophysics Source Code Library, ascl:1203.012
- Primini, F. A., & Kashyap, V. L. 2014, *ApJ*, **796**, 24
- Raskin, C., & Kasen, D. 2013, *ApJ*, **772**, 1
- Rau, U., & Cornwell, T. J. 2011, *A&A*, **532**, A71
- Roming, P. W. A., Kennedy, T. E., Mason, K. O., et al. 2005, *SSRv*, **120**, 95
- Russell, B. R., & Immler, S. 2012, *ApJL*, **748**, L29
- Ryder, S. D., Sadler, E. M., Subrahmanyam, R., et al. 2004, *MNRAS*, **349**, 1093
- Salas, P., Bauer, F. E., Stockdale, C., & Prieto, J. L. 2013, *MNRAS*, **428**, 1207
- Sand, D. J., Amaro, R. C., Moe, M., et al. 2019, *ApJL*, **877**, L4
- Sand, D. J., Graham, M. L., Botyánszki, J., et al. 2018, *ApJ*, **863**, 24
- Sand, D. J., Hsiao, E. Y., Banerjee, D. P. K., et al. 2016, *ApJL*, **822**, L16
- Schechter, P. L., Mateo, M., & Saha, A. 1993, *PASP*, **105**, 1342
- Schlaflly, E. F., & Finkbeiner, D. P. 2011, *ApJ*, **737**, 103
- Schmidt, G. D., Weymann, R. J., & Foltz, C. B. 1989, *PASP*, **101**, 713
- Sequist, E. R., & Taylor, A. R. 1990, *ApJ*, **349**, 313
- Shappee, B. J., Holoien, T. W. S., Drout, M. R., et al. 2019, *ApJ*, **870**, 13
- Shappee, B. J., Piro, A. L., Stanek, K. Z., et al. 2018, *ApJ*, **855**, 6
- Shappee, B. J., Stanek, K. Z., Pogge, R. W., & Garnavich, P. M. 2013, *ApJL*, **762**, L5
- Shen, K. J., & Bildsten, L. 2007, *ApJ*, **660**, 1444
- Shen, K. J., Bildsten, L., Kasen, D., & Quataert, E. 2012, *ApJ*, **748**, 35
- Shen, K. J., Guillochon, J., & Foley, R. J. 2013, *ApJL*, **770**, L35
- Smith, R. J., Lucey, J. R., Hudson, M. J., Schlegel, D. J., & Davies, R. L. 2000, *MNRAS*, **313**, 469
- Soderberg, A. M., Chevalier, R. A., Kulkarni, S. R., & Frail, D. A. 2006a, *ApJ*, **651**, 1005
- Soderberg, A. M., Nakar, E., Berger, E., & Kulkarni, S. R. 2006b, *ApJ*, **638**, 930
- Soker, N. 2019, *RNAAS*, **3**, 153
- Stauffer, C. M., Margutti, R., Linford, J. D., et al. 2021, *MNRAS*, **505**, 1153
- Swift, J., & Vynal, C. 2018, *RTSRE*, **1**, 281
- Szalai, T., Vinkó, J., Könyves-Tóth, R., et al. 2019, *ApJ*, **876**, 19
- Tartaglia, L., Sand, D. J., Valenti, S., et al. 2018, *ApJ*, **853**, 62
- Thielemann, F. K., Nomoto, K., & Yokoi, K. 1986, *A&A*, **158**, 17
- Thompson, T. A. 2011, *ApJ*, **741**, 82
- Tonry, J. L., Denneau, L., Heinze, A. N., et al. 2018, *PASP*, **130**, 064505
- Tucker, M. A., Ashall, C., Shappee, B. J., et al. 2021, *ApJ*, **914**, 50
- Tucker, M. A., Shappee, B. J., Vallely, P. J., et al. 2020, *MNRAS*, **493**, 1044
- Tucker, M. A., Shappee, B. J., & Wisniewski, J. P. 2019, *ApJL*, **872**, L22
- Valenti, S., Howell, D. A., Stritzinger, M. D., et al. 2016, *MNRAS*, **459**, 3939
- Valenti, S., Sand, D., Pastorello, A., et al. 2014, *MNRAS*, **438**, L101
- Vallely, P. J., Fausnaugh, M., Jha, S. W., et al. 2019, *MNRAS*, **487**, 2372
- Wang, L., Contreras, C., Hu, M., et al. 2020, *ApJ*, **904**, 14
- Wang, X., Filippenko, A. V., Ganeshalingam, M., et al. 2009, *ApJL*, **699**, L139
- Webbink, R. F. 1984, *ApJ*, **277**, 355
- Weiler, K. W., Williams, C. L., Panagia, N., et al. 2007, *ApJ*, **671**, 1959
- Whelan, J., & Iben, I., Jr. 1973, *ApJ*, **186**, 1007
- Wood-Vasey, W. M., & Sokoloski, J. L. 2006, *ApJL*, **645**, L53
- Woosley, S. E., & Weaver, T. A. 1994, *ApJ*, **423**, 371
- Yaron, O., Prialnik, D., Shara, M. M., & Kovetz, A. 2005, *ApJ*, **623**, 398
- Yoon, S. C., & Langer, N. 2005, *A&A*, **435**, 967
- Zacharias, N., Finch, C. T., Girard, T. M., et al. 2013, *AJ*, **145**, 44